The Homogenized Energy Model (HEM) for Characterizing Polarization and Strains in Hysteretic Ferroelectric Materials: Material Properties and Uniaxial Model Development

Ralph C. Smith and Zhengzheng Hu
Department of Mathematics
Center for Research in Scientific Computation
North Carolina State University
Raleigh, NC 27695

Abstract

Ferroelectric materials, such as PZT, PLZT and $BaTiO_3$, are being considered, or are already being employed, for a large number of applications including nanopositioning, high speed valves for fuel injectors, ultrasonic transducers, high speed camera shutters and auto focusing mechanisms, energy harvesting, and pico air vehicle design. Their advantages include nanometer positioning resolution, broadband frequency responses, moderate power requirements, the capability for miniaturization, and complementary actuator and sensor capabilities. However, they also exhibit creep, rate-dependent hysteresis, and constitutive nonlinearities at essentially all drive levels due to their noncentrosymmetric nature. In this paper, we model the hysteretic dependence of strains and polarization on input fields and stresses using the homogenized energy model (HEM) framework. At the domain level, the minimization of Gibbs energy densities yields linear constitutive relations. Nonlinearities and hysteresis due to dipole switching is modeled at the grain level by using Boltzmann theory to specify the evolution of dipole fractions which serve as internal variables. In the final step of the development, stochastic homogenization, based on the assumption that interaction fields and driving forces are manifestations of underlying densities, is used to construct nonlinear constitutive relations for the bulk material. It is demonstrated that these relations are amenable to subsequent development of distributed system models. The paper includes significant discussion regarding the mechanisms that produce hysteresis in ferroelectric materials. The capability of the framework for characterizing various hysteretic phenomena, including creep and various rate-dependencies, is illustrated by validation with PZT and PLZT data.

Report Documentation Page

Form Approved
OMB No. 0704-0188

1. REPORT DATE	2. REPORT TYPE	3. DATES COVERED
JAN 2012		**00-00-2012 to 00-00-2012**

4. TITLE AND SUBTITLE	5a. CONTRACT NUMBER
The Homogenized Energy Model (HEM) for Characterizing Polarization and Strains in Hysteretic Ferroelectric Materials: Material Properties and Uniaxial Model Development	5b. GRANT NUMBER
	5c. PROGRAM ELEMENT NUMBER
6. AUTHOR(S)	5d. PROJECT NUMBER
	5e. TASK NUMBER
	5f. WORK UNIT NUMBER
7. PERFORMING ORGANIZATION NAME(S) AND ADDRESS(ES) **North Carolina State University,Center for Research in Scientific Computation,Department of Mathematics,Raleigh,NC,27695-8212**	8. PERFORMING ORGANIZATION REPORT NUMBER **CRSC-TR12-01**
9. SPONSORING/MONITORING AGENCY NAME(S) AND ADDRESS(ES)	10. SPONSOR/MONITOR'S ACRONYM(S)
	11. SPONSOR/MONITOR'S REPORT NUMBER(S)

12. DISTRIBUTION/AVAILABILITY STATEMENT
Approved for public release; distribution unlimited

13. SUPPLEMENTARY NOTES

14. ABSTRACT

Ferroelectric materials, such as PZT, PLZT and BaTiO3, are being considered, or are already being employed, for a large number of applications including nanopositioning, high speed valves for fuel injectors, ultrasonic transducers, high speed camera shutters and auto focusing mechanisms energy harvesting, and pico air vehicle design. Their advantages include nanometer positioning resolution, broadband frequency responses, moderate power requirements, the capability for miniaturization and complementary actuator and sensor capabilities. However, they also exhibit creep rate-dependent hysteresis, and constitutive nonlinearities at essentially all drive levels due to their noncentrosymmetric nature. In this paper, we model the hysteretic dependence of strains and polarization on input fields and stresses using the homogenized energy model (HEM) framework. At the domain level, the minimization of Gibbs energy densities yields linear constitutive relations. Nonlinearities and hysteresis due to dipole switching is modeled at the grain level by using Boltzmann theory to specify the evolution of dipole fractions which serve as internal variables. In the final step of the development, stochastic homogenization, based on the assumption that interaction fields and driving forces are manifestations of underlying densities, is used to construct nonlinear constitutive relations for the bulk material. It is demonstrated that these relations are amenable to subsequent development of distributed system models. The paper includes significant discussion regarding the mechanisms that produce hysteresis in ferroelectric materials. The capability of the framework for characterizing various hysteretic phenomena, including creep and various rate-dependencies, is illustrated by validation with PZT and PLZT data.

15. SUBJECT TERMS

16. SECURITY CLASSIFICATION OF:			17. LIMITATION OF ABSTRACT	18. NUMBER OF PAGES	19a. NAME OF RESPONSIBLE PERSON
a. REPORT **unclassified**	b. ABSTRACT **unclassified**	c. THIS PAGE **unclassified**	**Same as Report (SAR)**	**49**	

Standard Form 298 (Rev. 8-98)
Prescribed by ANSI Std Z39-18

Nomenclature

d	Piezoelectric constant (m/V = C/N)
h	Piezoelectric constant (V/m = N/C)
E	Electric field (V/m)
g	Gibbs energy for dipoles (CV)
G_α	Gibbs energy density of α-variant (CV/m^3)
G^e_α	Electric Gibbs energy density of α-variant (CV/m^3)
P	Polarization (C/m^2)
$\overline{P}$	Polarization kernel (C/m^2)
P^α	Polarization of α-variant (C/m^2)
P^α_R	Remanent polarization of α-variant (C/m^2)
P^α_m	Minimum polarization of α-variant (C/m^2)
s^E_α	Elastic compliance of α-variant at constant field (m^2/N)
T	Temperature (K)
x_+, x_-, x_{90}	Fraction of positively, negatively and 90^o oriented dipoles (Unitless)
Y^P_α	Elastic stiffness of α-variant at constant polarization (N/m^2)
ϵ	Permittivity (F/m = C/Vm)
ε	Strain (Unitless)
$\overline{\varepsilon}$	Strain kernel
ε^α	Strain of α-variant
ε^α_R	Remanence strain of α-variant
ε^α_m	Minimum strain of α-variant
γ	$\gamma \equiv V/kT$
η^ε	Inverse susceptibility at constant strain (m/F = Vm/C)
σ	Stress (N/m^2)
τ_{90}, τ_{180}	Relaxation time for 90^o and 180^o switching (s)
χ_e	Electric susceptibility (Unitless)
χ^σ_α	Ferroelectric susceptibility of α-variant at constant stress (F/m = C/Vm)
ψ_α	Helmholtz energy density of α-variant (CV/m^3)

1 Introduction

Piezoelectric materials exhibit two complementary properties due to their noncentrosymmetric structure: the direct effect in which applied stresses generate an electric charge, and the converse effect in which applied fields produce deformations in the material. These properties respectively imbue the materials with sensor and actuator capabilities as well as the potential for self-sensing actuation. Commonly employed piezoelectric materials include barium titanate ($BaTiO_3$), lead zirconate titanate or PZT ($Pb(Ti_{1-x}Z_x)O_3$) lanthanum-doped lead zirconate titanate (PLZT), and piezoelectric polymers such as polyvinylidene fluoride (PVDF). For the PZT compounds, $x \in [0, 1]$ is chosen to optimize electromechanical coupling. Additionally, naturally occurring crystals such as quartz, sucrose (table sugar), and Rochelle salts, and biological materials such as bone exhibit piezoelectric effects to varying degrees. The actuator and sensor capabilities of quartz are exemplified by the fact that in 1916, Paul Langevin developed a quartz-based sonar transducer for submarine detection [64,75]. For present applications, however, we will focus on $BaTiO_3$, PZT, PLZT, PVDF and the electrostrictive material lead manganese niobate (PMN).

These materials are ferroelectric and hence exhibit a domain structure and spontaneous polarization at temperatures below the Curie point. The metastability associated with multiple stable dipole configurations produces hysteresis and constitutive nonlinearities in field-polarization and field-strain responses. In this paper, we focus on mechanisms that produce hysteresis in ferroelectric materials and the development of homogenized energy models that can be used for material characterization, device design, and model-based control design.

There exist a wide range of actuator and sensor designs with specific choices dictated by the application. Stacked actuators, such as that depicted in Figure 1(a), are employed in numerous applications including stages for atomic force microscopy and nanopositioners (see Figure 2), high speed valves for fuel injection, vibration control devices, depth finders and hydrophones, and linear and rotary piezomotors. Tube actuators comprise the active mechanisms in micropumps and scanning and atomic force microscopes. Bender-type transducers, such as the unimorph and bimorph designs depicted in Figure 1(c) and (d), are employed in pneumatic values, high speed camera shutters,

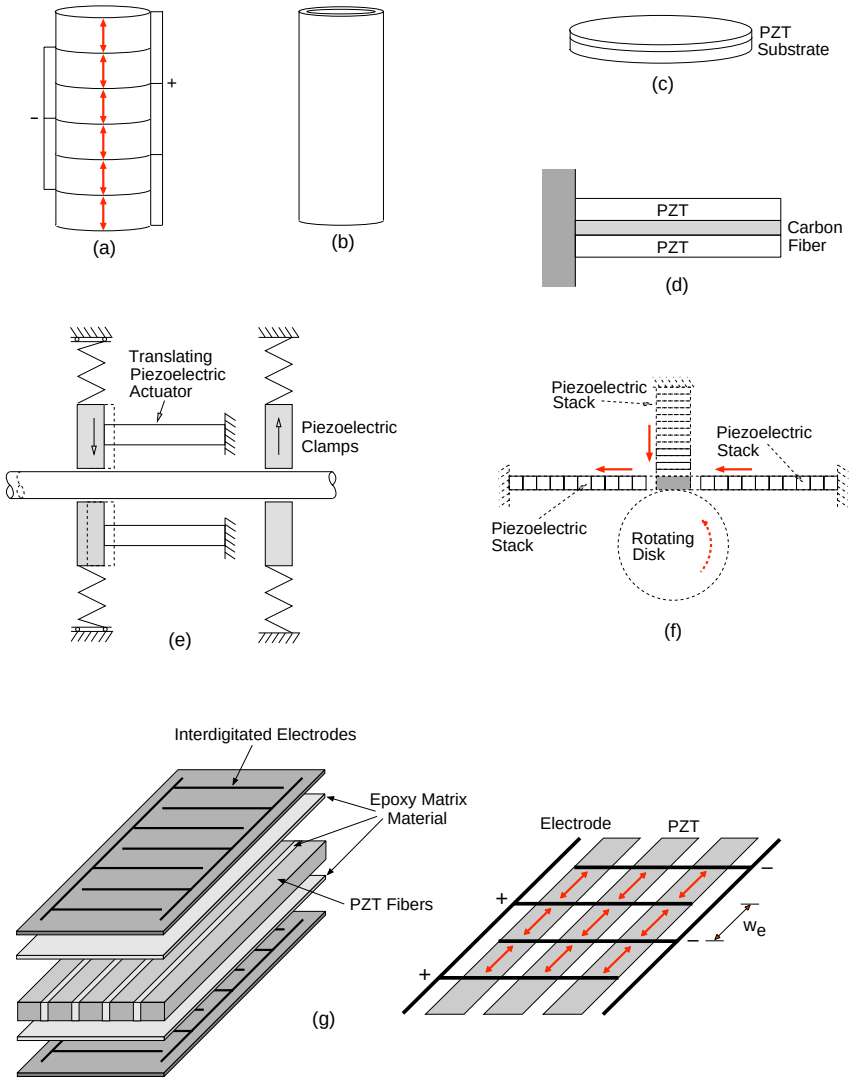

Figure 1: (a) Stack, (b) tube, (c) unimorph, and (d) bimorph transducers. (e) Linear and (f) rotary piezomotors. (g) Macro-fiber composite (MFC) transducer.

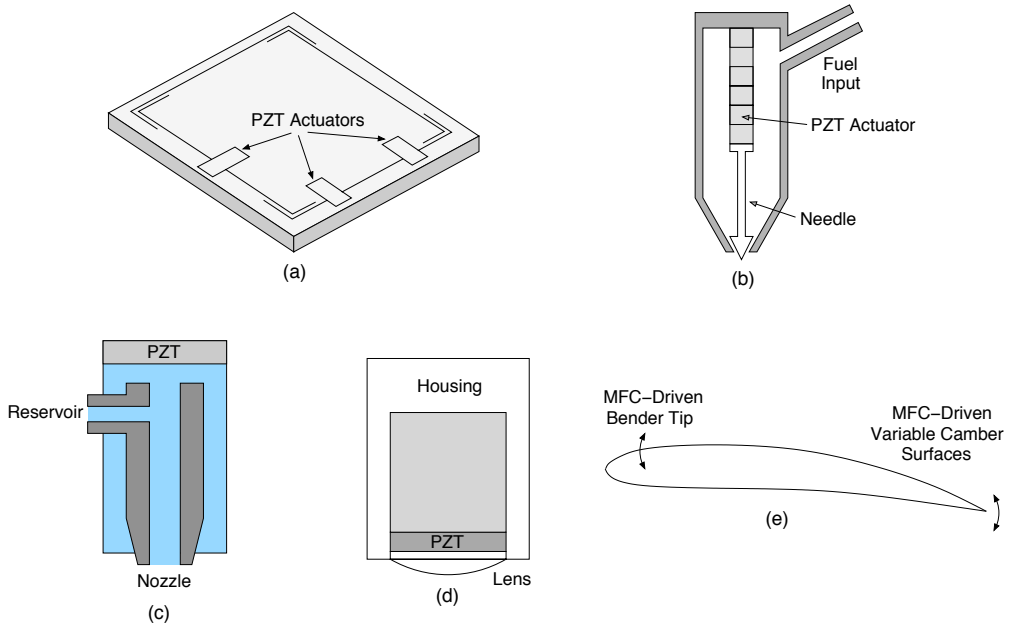

Figure 2: (a) Nanopositioning stage, (b) high speed valve for fuel injection, (c) inkjet printer nozzle, (d) ultrasonic transducer, and (e) MFC for shape modification and flow control.

energy harvesting devices, piezoelectric transformers, and inkjet printers (Figure 2(c)). Bimorphs are also employed as actuators for pico air vehicles such as the Harvard RoboBee [90] and both flying and ambulatory microrobots [28, 68, 91]. Bending-type PZT actuators are also employed in ultrasonic transducers for dental tools and biomedical imaging and treatment (Figure 2(d)). An emerging technology is MRI-guided focused ultrasound surgery in which high energy ultrasound waves are used to thermally ablate tumors and growths such as uterine fibroids. We note that ultrasonic devices operate at around 40 kHz whereas piezoelectric transformers operate in the 100 kHz to 1 MHz range thus demonstrating the high frequency capabilities of the materials. Solid state piezomotors are employed in applications such as camera auto-focusing mechanisms and medical equipment subject to large magnetic fields; e.g., small piezomotors for microsurgery and large motors to position positions in MRI environments. Macro-fiber composites (MFC), depicted in Figure 1(g), provide large strain and force capabilities in addition to durability and flexibility. They are presently being considered for applications including shape modification and flow control for micro-air vehicles (MAV) as well as energy harvesting in a range of environments [12,49,82]. Sensor applications include accelerometers, knock sensors to monitor engine combustion, pressure and force sensors, ultrasonic distance sensors, and vibration sensors to monitor automotive, railroad, and aircraft components. The direct piezoelectric effect is also utilized in high voltage spark igniters. Finally, 180^o switching in ferroelectric materials forms the basis for ferroelectric memory technologies (e.g., FeRAM) [70]. Additional discussion of applications can be found in [53, 67, 75, 85–87].

The advantages of piezoelectric actuators, sensors, and motors are due to a number of factors. They can be designed to provide nanometer positioning resolution and operate at frequencies ranging from DC to MHz. They have modest power requirements and do not create nor are they influenced by electromagnetic interference. Their solid state nature promotes miniaturization and simplified designs which improves product performance at reduced costs. They generate little heat, are non-flammable, and can be operated in a vacuum. Finally, the complementary direct and converse effects provide the materials and devices with multiple design properties including actuator, sensor, self-monitoring, nondestructive evaluation, and energy harvesting capabilities.

The price paid for the unique transducer capabilities of ferroelectric materials is hysteresis and constitutive nonlinearities due to the metastable behavior associated with inherent domain properties. Whereas these effects can be minimized using charge or current control [62], or restriction to low drive regimes, this can increase costs and limit the unique transduction capabilities of the materials. This necessitates the development of models and model-based control designs that quantify the nonlinear and hysteretic material behavior to achieve the full potential of the materials and devices.

Static, quasistatic, and dynamic hysteresis behavior that must be incorporated in models is illustrated in Figure 3. The field-polarization and field-strain data from [96] illustrates that rate-

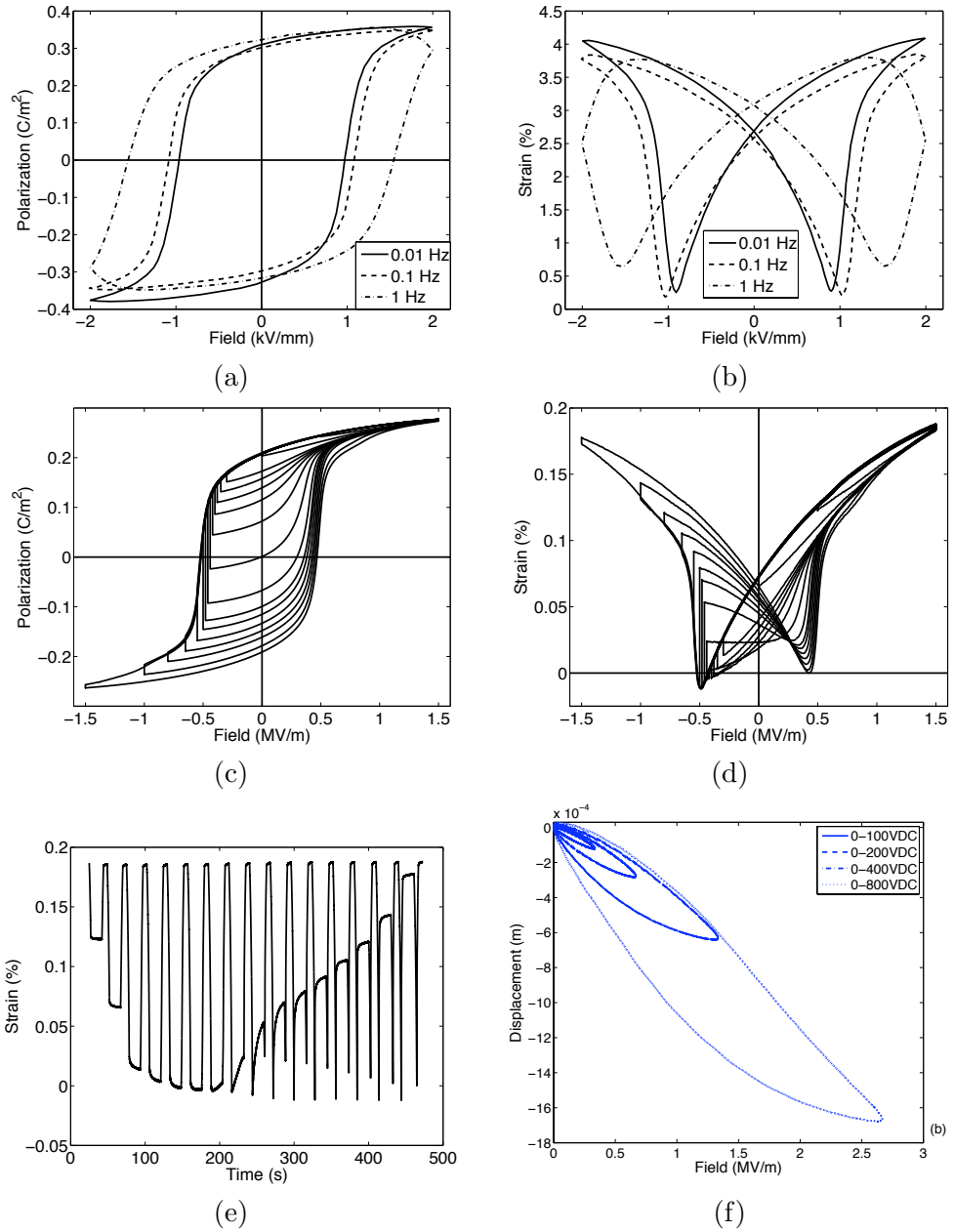

Figure 3: Rate-dependent (a) polarization and (b) strain PZT data from [96]. (c) Field-polarization, (d) field-strain and (e) time-strain PZT data from [92]. (f) Field-strain MFC data from [32].

dependent effects are significant at frequencies as low as 1 Hz. PZT data from [92] illustrates that for fixed field inputs, both the strain and polarization exhibit significant creep on timescales of 1 to 20 seconds. Finally, the MFC data from [32] illustrates nested minor loop behavior typical of moderate drive regimes. Whereas the full switching behavior shown in Figure 3(a)-(d) will typically not be encountered in applications, general models must account for the full range of rate-dependent and creep behavior to provide comprehensive device characterization.

For regimes in which stress and field inputs σ and E are maintained at low levels, the nonlinear and hysteretic behavior of the strain ε and polarization P can be approximated by the linear relations

$$\begin{aligned} P &= d\sigma + \chi^{\sigma} E \\ \varepsilon &= s^{E}\sigma + dE \end{aligned} \tag{1}$$

originally developed by Voigt [88]. Here d, χ^{σ} and s^{E} denote the piezoelectric constant, ferroelectric susceptibility at constant stress, and elastic compliance at constant field E. These are often termed the *piezoelectric relations* which infers a linear connotation on piezoelectric materials. This is somewhat of a misnomer since the piezoelectric materials $BaTiO_3$, PZT, PLZT, and PVDF are ferroelectric and hence exhibit hysteresis and constitutive nonlinearities. For some applications, however, the linear relations (1) provide sufficient accuracy, especially when combined with feedback algorithms.

To motivate various nonlinear modeling strategies, we consider the multiscale depiction of a PZT-based MFC tranducer in Figure 4. The largest scale is comprised of the application whereas initial characterization experiments are often conducted with individual MFC bonded to an elastic structure;

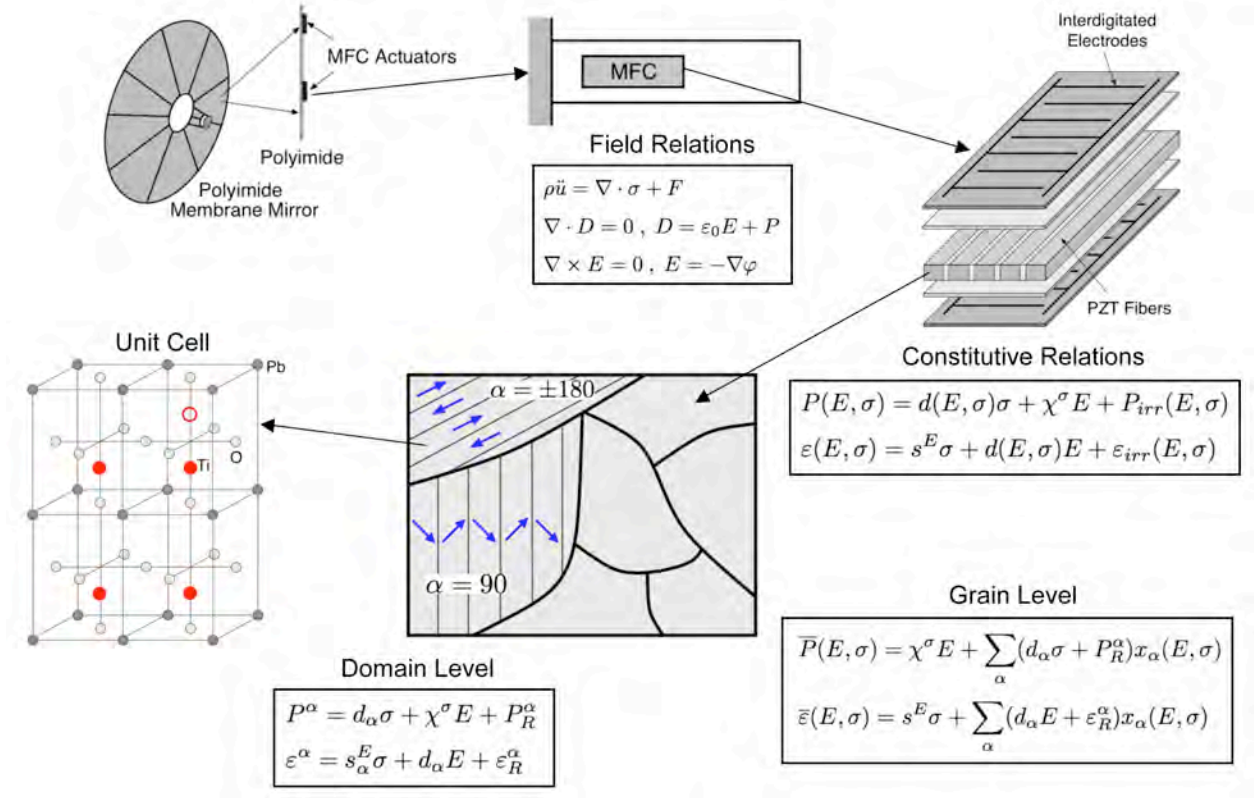

Figure 4: Multiscale behavior of a PZT-based MFC transducer at the application, device, material and unit cell levels.

e.g., a beam, plate or shell. The active component of the MFC is PZT fibers which are depicted at the material, grain, domain and unit cell levels. The goal for device optimization and control is to develop nonlinear, macroscale constitutive relations that can be employed in mechanical and electrostatic field relations which subsequently can be used to construct finite element simulation and control codes for the structure, device or application. The different modeling hierarchies are defined by the degree to which molecular, domain, and grain-level material behavior is used to construct the constitutive relations.

The general form of constitutive relations can be motivated by the ionic behavior of the unit cell. For small field or stress inputs, ionic displacements are reversible and approximately linear so they have the form

$$\begin{aligned} P^\alpha &= d_\alpha \sigma + \chi^\sigma_\alpha E + P^\alpha_R \\ \varepsilon^\alpha &= s^E_\alpha \sigma + d_\alpha E + \varepsilon^\alpha_R \end{aligned} \tag{2}$$

where α designates the dipole variant — e.g., $\pm 180, 90$ for tetragonal materials — and $P^\alpha_R, \varepsilon^\alpha_R$ are remanent values of the polarization and strain. At larger input levels, however, irreversible switching occurs which produces hysteresis and constitutive nonlinearities. This combination of reversible and irreversible behavior motivates the general constitutive formulation

$$\begin{aligned} P(E,\sigma) &= d(E,\sigma)\sigma + \chi^\sigma E + P_{irr}(E,\sigma) \\ \varepsilon(E,\sigma) &= s^E \sigma + d(E,\sigma)E + \varepsilon_{irr}(E,\sigma) \end{aligned} \tag{3}$$

where $d(E,\sigma), P_{irr}(E,\sigma)$ and $\varepsilon_{irr}(E,\sigma)$ incorporate the nonlinear and irreversible history-dependence due to dipole switching. We note that many authors employ the notation P^r, ε^r and terminology 'irreversible remanent behavior' but the concepts are the same.

Modeling hierarchies can generally be defined by the manner in which d, P_{irr} and ε_{irr} are constructed. Micromechanical, or microscopically-motivated models are based on an energy description of the material at the domain or grain level in combination with various homogenization techniques to provide expressions for the nonlinear, effective components d, P_{irr} and ε_{irr}. The objective is to let the micro-level physics inform, to the degree possible, resulting macroscale behavior. The difficulty with this approach is that resulting models are often too complex for applications requiring high speed implementation; recall that applications can occur at kHz rates. Phenomenological models circumvent the difficulties associated with quantifying complex, or poorly understood, micro-scale physics by constructing relations for d, P_{irr} and ε_{irr} based on macroscale observations or experimental measurements. In many models, the derivation of these effective components is guided by thermodynamic constraints, and the history-dependence associated with dipole switching is often incorporated with nonphysical internal variables. In general, phenomenological models are less complex than micromechanical models and hence are amenable to finite element implementation for devices and applications.

Micromechanical Models

As illustrated in Figure 4, microscopically-motivated or micromechanical models must incorporate two phenomena: a kinematic description of the grain-level irreversible or remanent polarization $\overline{P}_{irr}$ and strain $\overline{\varepsilon}_{irr}$,and criteria that quantify dipole switching. As detailed in the survey papers [33, 51] by Huber and Landis, many early papers [36, 60] assumed single domain behavior within single crystals, in which case, the remanent polarization and strain were simply the spontaneous polarization and strain. To account for multiple domains, which is always the case for ferroelectric materials, one must either track the nucleation and movement of domain walls, or account for their behavior using internal variables x_α, the most natural of which are volume or dipole fractions.

Phase field models, typically based on Ginzburg-Landau energy relations, provide one method for quantifying domain wall behavior [89]. As detailed in [75,81,95], the Ginzburg-Landau theory differs from the standard Landau relations through the inclusion of polarization gradient energy terms which incorporate local polarization changes associated with domain walls. This approach permits fundamental understanding of domain behavior but is typically too computationally intensive for use in macroscopic constitutive relations requiring high speed implementation. To reduce the number of parameters, continuum theories based on internal variables that quantify the polarization and strain state have been employed by a number of researchers — see [35] as well as the summary in [33, 51].

A variety of techniques have been employed to quantify dipole switching. Hwang et al. [36] introduced the concept of switching levels and a number of researchers have employed switching surfaces [73]. The homogenized energy model (HEM) framework, initially developed in [75, 78, 80] and extended here, quantifies switching through the evaluation of likelihoods that balance the Gibbs and relative thermal energy at the grain level.

We note that the kinetics associated with dipole switching determine the time scale for polarization and strain changes relative to mechanical and electrical loading rates. This is manifested in the rate-dependent hysteresis behavior observed in Figure 3 and illustrates that hysteresis involves multiple timescales as well as spatial scales.

A variety of techniques have been employed to average, or homogenize, grain-level relations to provide macroscale constitutive relations — e.g., see [33, 51]. This includes Reuss approximations, based on the assumption that stress and electrical fields are homogeneous throughout the polycrystal [36, 60], and various self-consistent averaging techniques [34, 35]. In the homogenized energy framework, this is accomplished by assuming that quantities such as effective and interaction fields are manifestations of underlying densities that are subsequently estimated through fits to measured macroscopic data. The assumptions and techniques used to homogenize from the grain to macro-level often determine the accuracy and efficiency of the resulting model.

We note that this summarizes only a few of the issues addressed by micromechanical models and other research has focused on the quantification of field and stress interactions between grains [73], the incorporation of friction effects in domain wall movement [74], micromechanics models based on irreversible thermodynamics principles [38,83], and direct finite element implementation of micromechanics models [37].

In this summary, we have neglected the discussion of atomistic models that quantify material behavior at the level of the unit cell. This comprises a critical research area for understanding fundamental material properties and for designing new materials. However, it is generally too computationally intensive for direct macroscopic material characterization so we instead refer the reader to [11] for an overview of associated models.

Phenomenological Models

The goal when developing phenomenological models is to reduce complexity and often ensure thermodynamic consistency by constructing appropriate relations for d, P_{irr} and ε_{irr} based on attributes of measured data. The reader is referred to [42, 51, 65] for overviews of certain phenomenological frameworks.

In a number of models, the remanent or irreversible polarizations and strains are expressed in terms of nonphysical internal variables, often chosen to satisfy tenets of irreversible thermodynamics [19,44] or emulate theory of metal plasticity [45,52]. A number of these models have led to successful finite element implementation [42, 43, 50, 56, 59].

More recently, investigations have focused on representing d, P_{irr} and ε_{irr} in terms of Preisach operators [41], Jiles-Atheron hysteresis relations [27] and hysteretic recurrent neural networks [57].

The Prandtl-Ishlinskii (PI) hysteresis operator is also receiving significant attention since it can be proven that its inverse is also a Prandtl-Ishlinskii operator [14]. Whereas the classical PI operator, like the Preisach operator for which it is a subset, is symmetric and rate-independent, recent extensions to the theory address asymmetry, rate-dependence and certain creep phenomena [2,3,48]. Although these extensions complicate the construction of inverse models, the PI model, along with the Preisach and homogenized energy frameworks, provides a feasible avenue for feedforward control designs based on inverse models. Finally, we note that both the Preisach and PI models can be viewed as multiscale models in which kernels, or hysterons, phenomenologically describe grain-level behavior and homogenization to macroscales is achieved through integration against density functions.

Whereas there exist a number of rate-independent models, there are substantially fewer models that are capable of modeling rate-dependent phenomena such as that shown in Figure 3. The extended Preisach-PI formulation [48] quantifies certain rate-dependent material behavior as does the variational formulation [65] and models of [5,9] which incorporate kinetic theory to characterize rate-dependent loading effects. The homogenized energy model (HEM), which is the topic of this paper, quantifies rate-dependent effects based on evolution equations in combination with the theory of thermally activated processes.

Homogenized Energy Model (HEM)

The homogenized energy model is a multiscale, microscopically-motivated or micromechanical approach in the sense that it begins with energy analysis at the domain level to construct local constitutive relations (2). To construct the grain-level expressions

$$\begin{aligned} \overline{P}(E,\sigma) &= \sigma \sum_{\alpha} d_\alpha x_\alpha(E,\sigma) + \chi^\sigma E + \sum_{\alpha} P_R^\alpha x_\alpha(E,\sigma) \\ \overline{\varepsilon}(E,\sigma) &= s^E \sigma + E \sum_{\alpha} d_\alpha x_\alpha(E,\sigma) + \sum_{\alpha} \varepsilon_R^\alpha x_\alpha(E,\sigma), \end{aligned} \tag{4}$$

the internal variables x_α are chosen to be the fraction of α-variant dipoles; e.g., $\alpha = \pm 180, 90$ for tetragonal materials. The dynamics of x_α are governed by evolution equations driven by likelihoods constructed using Boltzmann theory to quantify the scaled probability of transitioning between stable equilibria associated with dipole variants. This incorporates the rate-dependence and multiple-time scales exhibited by the data in Figure 3.

For homogeneous single crystals with negligible interaction fields, these relations can adequately quantify macroscale behavior. For polycrystalline materials and single crystals with non-negligible interaction fields, macroscale models are constructed by assuming that properties such as coercive fields, critical driving forces, and interaction fields are manifestations of underlying densities rather than constants. This yields a homogenized energy framework that accurately characterizes a range of material behavior while retaining the efficiency required for data-driven parameter estimation, uncertainty quantification, design, and real-time model-based control implementation.

The framework was proposed in [75,78–80] for 180^o ferroelectric switching and extended in [7,71] to include 90^o ferroelastic switching. In both cases, transition likelihoods were constructed using the theory of thermally activated processes as originally applied to shape memory alloys in [1,72] and magnetic materials in [76,77]. It is shown in [75,79] that it thus provides a unified framework for characterizing hysteresis in ferroic materials. This approach has a strong theoretic basis and provides accurate and efficient characterization of 1-D ferroelectric switching but becomes increasingly slow to implement for ferroelastic and 3-D ferroelectric switching due to complications associated with computing inflection points and curves on 2-D and 3-D energy landscapes having 4-6 local minima. To address this, York used the driving force between local minima to construct mesoscale kernels for 1-D

PZT with ferroelastic switching [92] whereas Kim and Seelecke employed this technique to construct a 3-D electromechanical model [47]. York incorporated certain material and field nonhomogeneities within the hysteron and Kim modeled certain polycrystalline behavior using a representative volume element (RVE) model [46]. However, the combination of the driving force likelihood relations with stochastic homogenization to construct general macroscopic models for polycrystalline materials has not been previously investigated.

The novel contributions and organization of the paper can be summarized as follows. In Section 2, we provide a comprehensive discussion of the dipole processes that produce hysteresis and constitutive nonlinearities in ferroelectric materials. Whereas much of this material is classical, we focus on providing a careful discussion regarding the sources and mechanisms leading to even-powered (e.g, quadratic) field-strain effects since this is important for model development and is often ambiguous or contradictory in the literature. In Section 3, we summarize the 180^o polarization model that was originally proposed in [78, 80]. The novel component of this section is Section 3.2 in which we rigorously derive likelihood relations based on Boltzmann theory. This motivates alternative likelihood formulations based on activation energies and thermodynamic driving forces. Section 4 contains a derivation of the strain-polarization models based on both 180^o and non-180^o switching. The grain-level analysis is similar to that in [47,92] but the development of macroscopic models based on the homogenized energy framework is new. In Section 4.2, we show that the framework yields constitutive relations of the form (3) where $d(E,\sigma), P_{irr}(E,\sigma)$ and $\varepsilon_{irr}(E,\sigma)$ are homogenized or averaged relations employing the kernel expressions (4). This framework is then used in Section 5.1 to derive a lumped actuator model as well as constitutive relations for distributed systems. The performance of the model, for characterizing creep behavior and rate-dependent phenomena such as that shown in Figure 3, is demonstrated in Section 6.

It is shown in the companion paper [31] that due to its energy basis, the model admits highly efficient implementation and data-driven algorithms to determine initial parameter estimates based on measured properties of the data. This facilitates model calibration and implementation for design and control of devices and complex structures arising in applications. The model's feasibility for control applications is further bolstered by the fact that robust inverse model algorithms can be implemented at rates that are proven no slower than 1/6-1/7 the rate of forward algorithms. Finally, the unified nature of the framework facilitates its extension to magnetic, shape memory alloy, or hybrid systems.

2 Ferroelectric Materials

As detailed in Section 1, commonly employed transducer materials include $BaTiO_3$, PZT, PLZT, PMN and PVDF. Whereas the specific molecular mechanisms are material-dependent, all of these compounds exhibit certain shared meso- and macro-scale properties which form the basis for homogenized energy models. In this section, we summarize relevant material properties; we refer the reader to [40, 58, 66, 75] for details.

Barium titanate and lead titanate ($PbTiO_3$) are isostructural with the mineral perovskite ($CaTiO_3$) and exhibit what is termed a ABO_3 perovskite structure. As illustrated in Figure 5 for $BaTiO_3$, this consists of a paraelectric non-polar cubic structure above the Curie point T_c and ferroelectric tetragonal, orthorhombic, and rhombohedral forms at temperature below T_c. It is noted that for typical operating temperatures, $BaTiO_3$ and $PbTiO_3$ exhibit tetragonal structures whereas the composition 8/65/35 PLZT ($Pb_{0.08}Ti_{.35}Zr_{.65}O_3$) is near a rhombohedral-tetragonal morphotropic phase boundary and $PbZrO_3$ is orthorhombic. We will focus primarily on tetragonal structures but analogous results hold for rhombohedral and orthorhombic forms.

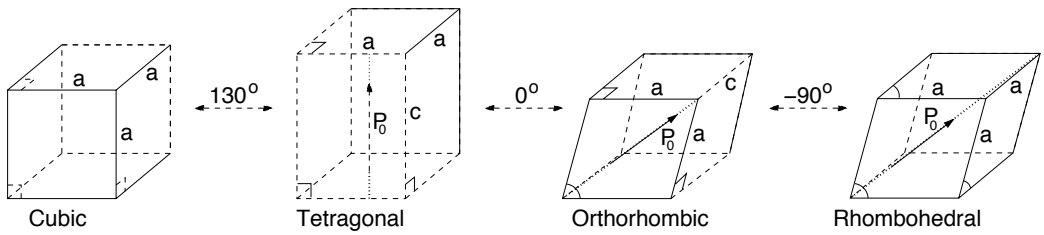

Figure 5: Cubic, tetragonal, orthorhombic and rhombohedral forms of perovskite compounds and approximate transition temperatures for $BaTiO_3$ (^oC).

As illustrated in Figure 6 for $BaTiO_3$, the materials exhibit a spontaneous polarization P_0 for $T < T_c$. This leads to to 180^o ferroelectric switching for fields greater than a coercive field E_c and 90^o ferroelastic switching for compressive stresses larger than a coercive stress σ_c. Both effects can occur in transducers and for devices, such as THUNDER, that exhibit large internal prestresses, both effects may be significant.

The electromechanical properties of ferroelectric compounds are intimately related to the manner in which the polar tetragonal, orthorhombic or rhombohedral structures respond to input fields and stresses. To illustrate these effects, we summarize the polarization and strain behavior for three cases: (i) single crystal, 180^o ferroelectric domains, (ii) single crystal, 180^o ferroelectric and 90^o ferroelastic domains, and (iii) polycrystalline materials.

Single Crystal, 180^o Ferroelectric Domains

In the absence of applied or internal stresses, minimization of the electrostatic energy yields twinned 180^o domains. For fields E less in magnitude than the coercive field E_c, this yields approximately linear E-P, E-ε, P-ε, where ε is the strain, behavior as illustrated in Figure 7. This is due to reversible deformations of the tetragonal cell and resulting strains are small compared to those resulting from 90^o switching. Fields in excess of E_c produce 180^o switching which yields large changes in polarization but small changes in strains since differences in the latter are due only to small changes in the cell dimension.

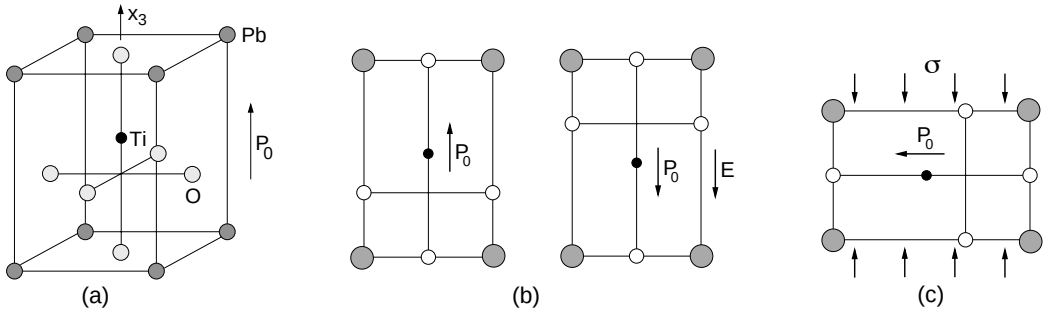

Figure 6: (a) Tetragonal structure of $PbTiO_3$ for $T < T_c$ and resulting spontaneous polarization P_0. (b) Ferroelectric 180^o polarization switch due to an applied electric field $E > E_c$ and (c) ferroelastic 90^o degree switch due to a compressive force σ larger in magnitude than the coercive stress σ_c.

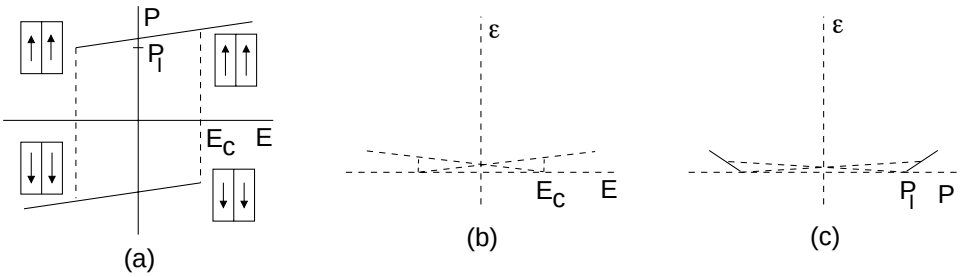

Figure 7: (a) Polarization changes due to 180^o ferroelectric dipole switching, and (b), (c) small strains resulting from deformations of the unit cell.

Single Crystal, 180^o Ferroelectric and 90^o Ferroelastic Domains

The situation is more complicated when fields and stresses are simultaneously applied to the materials. We illustrate the case of compressive stresses since this induces dipole switching. However, transducers such as macro-fiber composites (MFC) and THUNDER will exhibit regions having both tensile and compressive stresses.

We first note that the strains resulting from 90^o switching are significantly larger than the linear strains resulting from reversible deformations of the unit cell. For $BaTiO_3$ single crystals, this 90^o switching can produce strains up to 1.1%. The reader is referred to [15] for experimental results illustrating the E-P, E-ε and P-ε behavior of single crystal $BaTiO_3$ subject to various prestress levels. The behavior for $\sigma = -1.78$ MPa is plotted in Figure 11(a)-(c).

In Figure 8, we illustrate ferroelastic switching for an ideal single crystal. As compressive stresses are increased, two mechanisms produce changes in the strains and polarization: (i) linear elastic changes in the tetragonal cell, and (ii) nucleation and growth of 90^o domains. The primary 90^o rotation occurs at the coercive stress σ_c after which, the elastic stiffness $c = \frac{d\sigma}{d\varepsilon}$ is approximately linear. Representative domain configurations are shown in Figure 8(c).

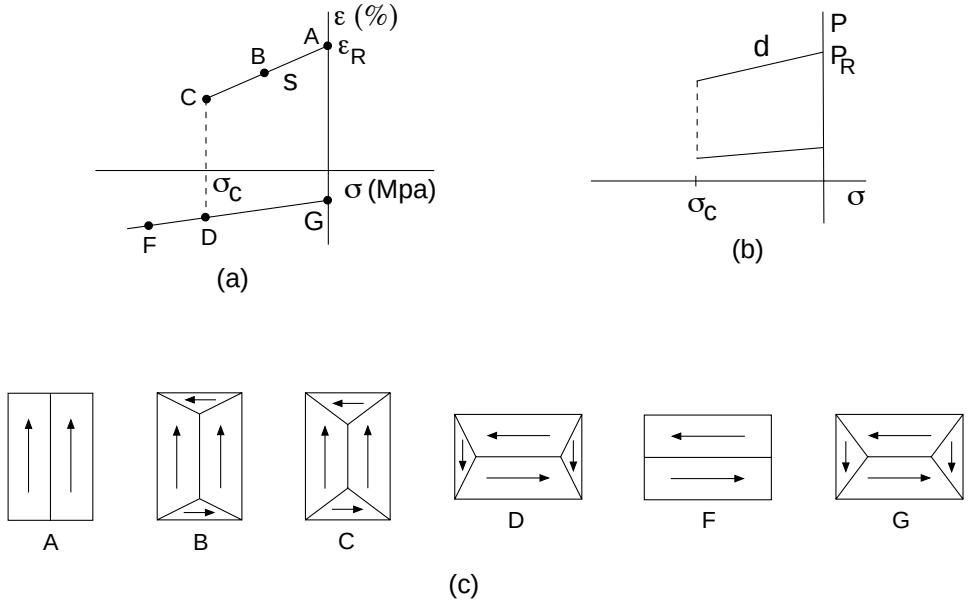

Figure 8: (a) and (b) Elastic response and stress-induced ferroelastic switch at σ_c for $E = 0$. (c) Nucleation and growth of 90^o domains during the switching process.

The E-P, E-ε and P-ε behavior at the points B and F corresponding to fixed stresses $\sigma \in (-\sigma_c, 0)$ and $\sigma \in (-\infty, -\sigma_c)$ are depicted in Figure 9. A comparison between Figure 9(a) and Figure 7 ($\sigma = 0$) illustrates that for $\sigma \in (-\sigma_c, 0)$, the magnitude of the polarization remains approximately the same but the behavior near coercivity reflects the 90^o switching. The strains are significantly larger due to the 90^o switching as demonstrated by experimental $BaTiO_3$ data in [15]. This regime provides optimal performance for single crystal actuators.

For fixed prestresses larger in magnitude than σ_c, ferroelastic switching yields 90^o domains as a starting state for $E = 0$ and the material behaves in a linear elastic manner until field-induced 90^o switching occurs at the point ii shown in Figure 9(b). Due to the magnitude of the prestresses, large fields E are required to produce significant polarization and strain levels and single crystal actuators operating in these regimes would have diminished outputs — or would be destroyed by internal field and stress levels.

Polycrystalline Materials

Whereas single crystal $BaTiO_3$ is being considered for applications, most ferroelectric transducer materials, such as PZT, are polycrystalline which affects their behavior in a variety of ways. It is first noted that whereas a single crystal is polar for $T < T_c$, polycrystalline compounds exhibit zero

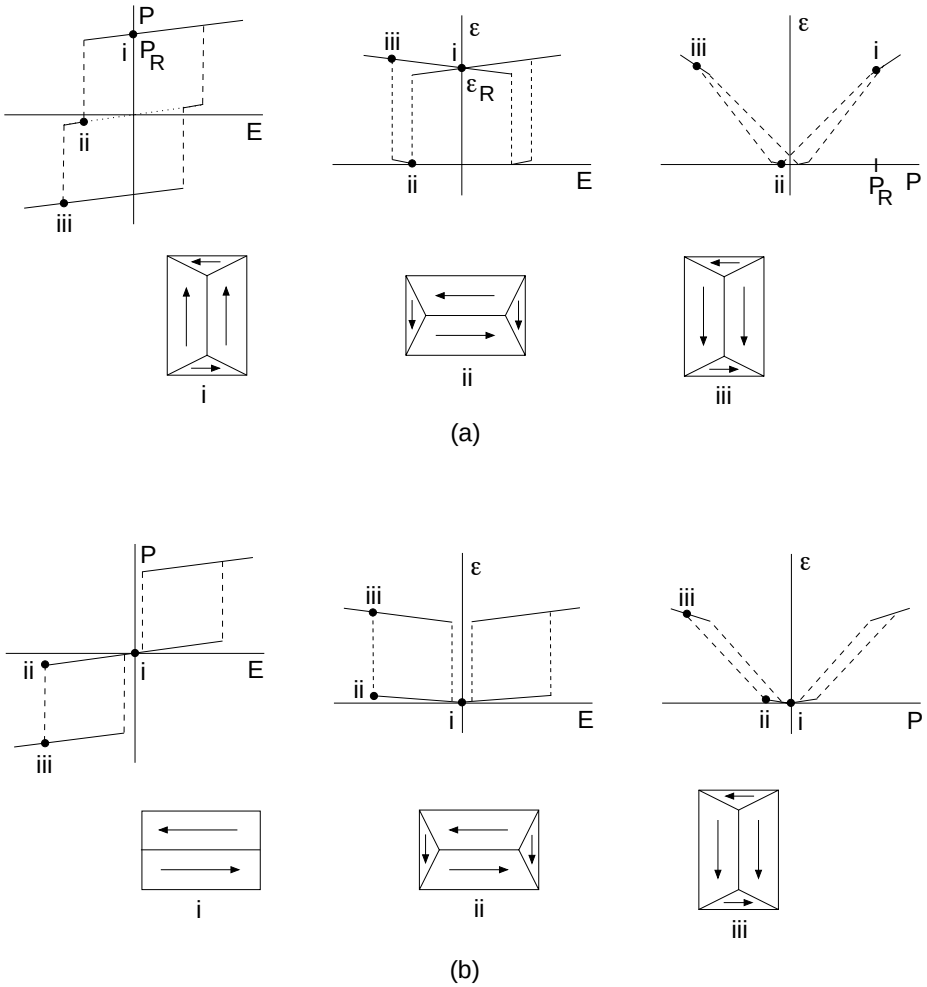

Figure 9: E-P, E-ε and P-ε behavior at fixed stresses σ corresponding to the points (a) B and (b) F from Figure 8. Field levels in (b) are larger than those in (a).

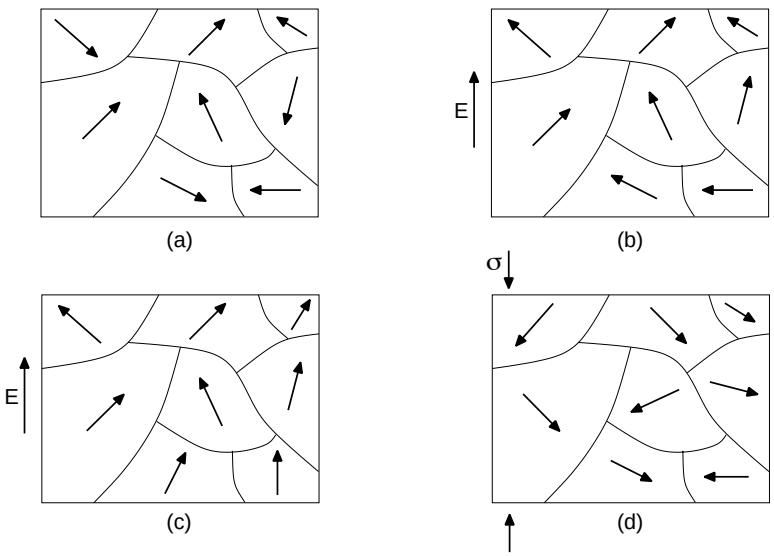

Figure 10: (a) Unpoled material, (b) rotation of 180^o domains due to poling, and (c) 90^o switching due to an applied field. (d) Ferroelastic 90^o switching due to an applied stress.

net polarization due to the random orientation of grains and domains. This necessitates that the materials be poled before use as illustrated in Figure 10(b) and (c). Due to the random orientation of grains, the materials exhibit smaller remanence polarizations than corresponding single crystals. Moreover, as shown in Figure 10(c), polycrystalline materials exhibit field-induced 90^o switching in the absence of a prestress and both 90^o and 180^o switching can occur at stresses and fields below single crystal coercive values. This causes polycrystalline E-P, E-ε and P-ε hysteresis curves to be smoother than their single crystal counterparts and it motivates the use of models such as the homogenized energy model, Preisach formulations or Prandtl-Ishlinskii models that can accommodate the random grain orientations via densities in the representation.

Polycrystalline PLZT data, corresponding to the ideal single crystal behavior depicted in Figures 8 and 9, can be found in [61]. Single crystal $BaTiO_3$ data from [15], polycrystalline PZT data from [92], PLZT data from [69], and PMN data from [29] are plotted in Figure 11. It is first noted that polycrystalline switching behavior is smoother than for $BaTiO_3$ single crystal due to material nonhomogeneities. It is also observed that PLZT exhibits nearly quadratic D-E behavior and PMN exhibits nearly quadratic and anhysteretic E-ε behavior as compared with the butterfly curves measured for PZT. We provide further discussion regarding the piezoelectric, quadratic, and switching behavior of these compounds in the next subsection.

2.1 Piezoelectric, Electrostrictive and Domain Switching Behavior

Ferroelectric materials exhibit a complex combination of linear, quadratic or quartic, and hysteretic behavior in general operating regimes. These effects are often categorized as piezoelectric, electrostrictive, or domain switching in nature but there is significant interplay between the underlying mechanisms and hence ambiguity in the definitions of the phenomena. We detail aspects of these phenomena to clarify the underlying physical mechanisms and motivate issue that must be addressed in models.

The direct piezoelectric effect constitutes the change in polarity that results from an applied stress whereas the converse piezoelectric effect constitutes reversible strains generated by applied field. In both cases, the designation piezoelectric has a linear connotation.

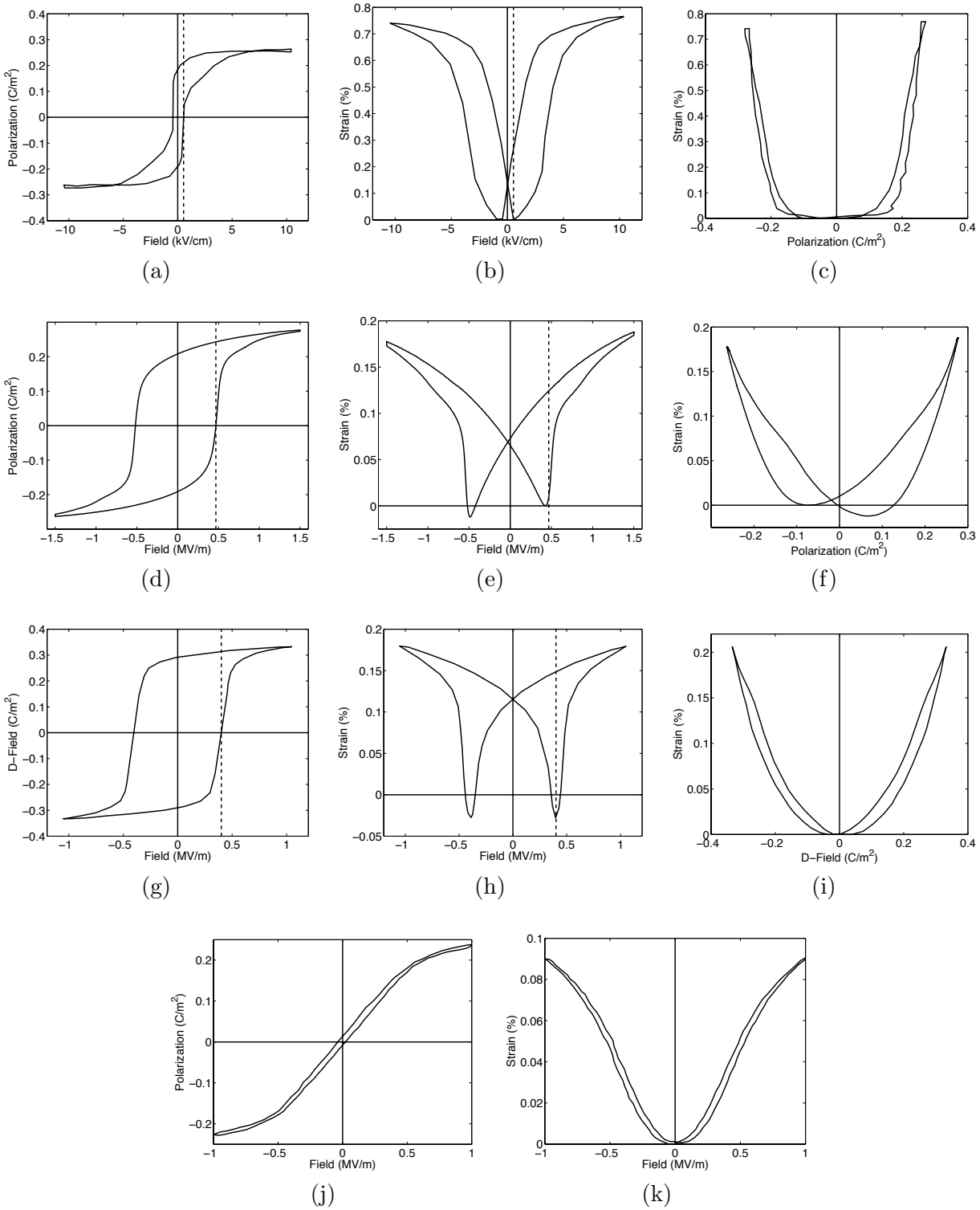

Figure 11: (a) E-P, (b) E-ε and (c) P-ε behavior of prestressed single crystal $BaTiO_3$ data from [15]. (d) E-P, (e) E-ε, and (f) P-ε behavior of PZT data from [92]. (g) E-D, (h) E-ε, and (i) D-ε behavior of PLZT data from [69]. (j) E-P and (k) E-ε behavior of PMN data from [29].

Electrostriction is classically used to designate field-induced strains that are proportional to even powers of the field and hence are independent of its polarity. Classical electrostriction results from reversible, and hence anhysteretic, deformations in the lattice structure and it is inherent to all materials including gaseous, liquid, and crystalline or amorphic, polar or centrosymmetric solids [16, 40, 58, 66]. In most ferroelectric materials, electrostrictive effects are small compared to linear piezoelectric effects and are hence neglected. However, in some compounds such as PMN, it is significant and must be included in models. Depending on the independent variables, electrostriction can be modeled as a quadratic, or higher-order, relation

$$\varepsilon = ME^2 \ , \ \varepsilon = QP^2 \ , \ \varepsilon = QD^2$$

between fields E, polarization P, or D-fields and the resulting strain ε.

A source of confusion stems from the fact that the quadratic dependence of strains on P, E or D is due to two different mechanisms: classical electrostriction and domain rotation. As noted previously, electrostriction results from reversible deformations of the lattice structure; hence it is anhysteretic and it occurs to varying degrees in all materials. In ferroelectric materials, domain rotation only occurs for $T < T_c$ when the material is in a polar state. The quadratic strains due to domain rotation are typically larger than electrostrictive effects, except in materials such as PMN, and $E - \varepsilon$ curves exhibit hysteresis. The difference between the nearly anhysteretic, electrostrictive, behavior of PMN and the hysteretic, domain switching, behavior of PZT and PLZT is illustrated in Figure 11.

We note that some researchers define quadratic effects due to domain reorientation as electrostriction [84] whereas others more generally define electrostriction as field-induced strains that are independent of the field polarity. We follow instead the distinction made by Caspari and Merz [17] between classical electrostriction and quadratic domain rotation effects since the two are characterized differently in the homogenized energy model.

We next detail why domain reorientation produces quadratic strain dependencies and then illustrate the relative contributions of electrostriction and quadratic domain reorientation for common ferroelectric materials.

Quadratic Strains Due to Domain Rotation

To illustrate how domain rotation can produce quadratic strains, we represent paraelectric cubic regions by unit spheres and the ferroelectric polar regions by ellipsoids as motivated by analysis of magnetostriction presented on pages 343–346 of [18] or pages 99–104 of [39]. We let $\bar{\varepsilon}$ denote the spontaneous strain generated by the paraelectric to ferroelectric phase transition when all dipoles are aligned with the field. As depicted in Figure 12(a), the strain at the angle θ is thus

$$\varepsilon(\theta) = \bar{\varepsilon} \cos^2 \theta. \tag{5}$$

For a random domain orientation, the spontaneous strain for the polarized material is thus

$$\lambda_0 = \int_0^{\pi/2} \bar{\varepsilon} \cos^2 \theta \sin \theta d\theta = \frac{\bar{\varepsilon}}{3}.$$

The application of a field causes domains to rotate in the manner depicted in Figure 12(c) thus yielding the relative change in dimension $\lambda_s = \bar{\varepsilon} - \lambda_0 = \frac{2}{3}\bar{\varepsilon}$. If we assume that changes in polarization are solely due to rotation, substitution of the relation $P = P_0 \cos\theta$ and $\bar{\varepsilon} = \frac{3}{2}\lambda_0$ into (5) yields the quadratic strain relation

$$\varepsilon(P) = \frac{3}{2} \frac{\lambda_s}{P_0^2} P^2.$$

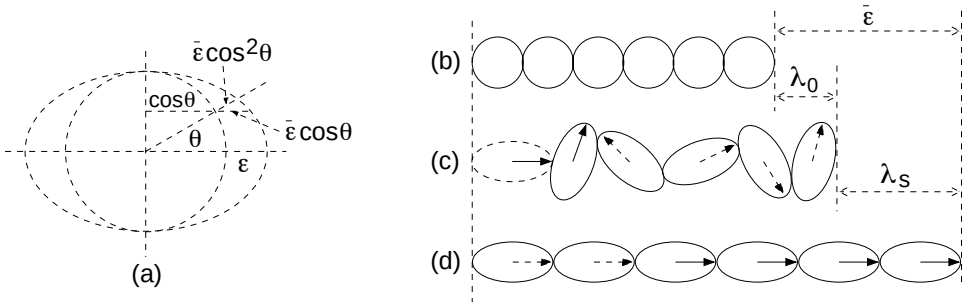

Figure 12: (a) Spontaneous strain as a function of the angle θ. (b) Spheres used to model isotropic, disordered material behavior in the paraelectric phase and (c) ellipsoids representing the order encapsulated by domains for $T < T_c$. (d) Total strain ε and strain λ_s due to orientation of domains in the field direction.

2.2 Material Behavior

Magnesium Niobate Compounds

As detailed in [75], PMN-PT-BT transducers are employed in applications including sonar transduction due to their low hysteresis, high strain capabilities. These relaxor ferroelectric compounds also exhibit significant electrostrictive behavior as illustrated in Figure 11(j)-(k) with data from [29]. For an operating temperature of 5^o C, the material exhibits nearly quadratic E-ε behavior at low to moderate field inputs and even, higher-order behavior at high fields. This provides a benchmark for discussing the degree to which electrostriction plays a role in $BaTiO_3$, PZT and PLZT behavior.

Single Crystal Barium Titanate

The behavior of $BaTiO_3$ has been heavily studied for over 60 years and it remains an important research topic due to the capability of single crystals to generate large strains ($\sim$1 %) through 90^o rotations. The behavior of single crystal $BaTiO_3$ subjected to various compressive stresses has recently been investigated in [15] and representative results are shown in Figure 11(a)-(c). It is observed that in contrast to PMN-PT-BT, the $BaTiO_3$ E-ε curve exhibits significant hysteresis which gives it a classical butterfly profile. Early authors attributed this to electrostrictive effects [63] but analysis originating in the classic 1950 paper by Caspari and Merz [17] demonstrates that it is primarily due to domain reorientation. This is the source of the hysteresis.

In [17], Caspari and Merz show that there are three sources of quadratic strain effects in $BaTiO_3$: spontaneous strains $\varepsilon_0 = QP_0^2$ resulting from the paraelectric to ferroelectric phase transition, butterfly effects due to dipole switching, and classical electrostrictive effects. To analyze the relative contribution due to electrostriction, they consider the field-induced strains ε that result when the polarization is biased about the spontaneous polarization P_0 and corresponding field E_0 as depicted in Figure 13. Application of an external field yields a change $\Delta\varepsilon$ in the strain so that

$$\varepsilon = \varepsilon_0 + \Delta\varepsilon = Q(P_0 + P)^2$$
$$\Rightarrow \Delta\varepsilon = (2QP_0)P + QP^2.$$

If we take $P = \chi E$, the change in strain can be expressed as

$$\Delta\varepsilon = (2Q\chi P_0)E + (Q\chi^2)E^2.$$

It follows that the piezoelectric constants g and d and the electrostrictive constant M are given by

$$g = 2QP_0\ ,\ d = 2Q\chi P_0\ ,\ M = Q\chi^2.$$

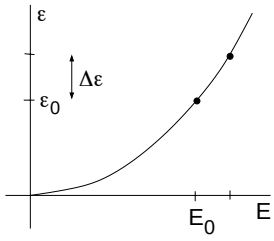

Figure 13: Change in strain $\Delta\varepsilon$ due to applied field increments about $E_0 = P_0/\chi$.

For the cgs parameter values given in [17], it is unfortunately difficult to directly compute the relative strain contributions. Instead, we use the following parameter values from [8] — see also [55] —

$$
\begin{aligned}
&Q = 0.11 \text{ m}^4/\text{C}^2 \\
&P_0 = 0.26 \text{ C/m}^2 \\
&\chi = \epsilon_0 \chi_e = 9.56 \times 10^{-10} \text{ C/(Vm)} \ , \ \chi_e = \epsilon_r - 1 \ , \ \epsilon_r = 109
\end{aligned}
$$

which yields

$$
\begin{aligned}
&g = 5.72 \times 10^{-2} \text{ m}^2/\text{C} \quad , \quad \text{[8] report } 5.75 \times 10^{-2} \text{ m}^2/\text{C measured} \\
&d = 5.47 \times 10^{-11} \text{ m/V} \quad , \quad \text{[8] report } 8.56 \times 10^{-11} \text{ m/V measured} \\
&M = 1.01 \times 10^{-19} \text{ m}^2/\text{V}^2.
\end{aligned}
$$

For a change in polarization $P = 0.05$ C/m^2 and field $E = 5 \times 10^5$ V/m, which is representative of the data in [15], this yields the strain contributions

$$
\begin{aligned}
gP = 2.86 \times 10^{-3} \quad &, \quad QP^2 = 2.75 \times 10^{-4} \\
dE = 2.74 \times 10^{-5} \quad &, \quad ME^2 = 2.53 \times 10^{-8}.
\end{aligned}
$$

In both cases, the quadratic electrostrictive effects are negligible compared with the linear piezoelectric effects and hence can be neglected. This implies that the piezoelectric effect can be interpreted as the electrostrictive effect biased about the spontaneous polarization P_0. It further implies that the E-ε and P-ε behavior shown in Figure 11(a)-(c), which is independent of field polarity, is due to the 90^o and 180^o switching which imbues the material with large strain capabilities. The P-ε behavior in Figure 11(c) also demonstrates that 180^o and 90^o switching for $BaTiO_3$ occur on very different timescales. The flat region indicates that 180^o polarization switching occurs in advance of strain-producing 90^o switches. It is shown in Section 3.3 and [31] that single crystal behavior of this type can be modeled using energy relations that incorporate both 90^o and 180^o switching mechanisms and employ linear domain-level constitutive relations.

Polycrystalline Tetragonal PZT and PL8ZT

As illustrated in Figure 10, polycrystalline compounds exhibit 90^o switching in the absence of applied stresses and at low field levels. To quantify the role of 90^o switching in polycrystalline compounds, Tsurumi et al. employed X-ray diffraction (XRD) techniques to measure the amount of 90^o reorientation [84]. We note that the PL8ZT compounds under consideration had chemical compositions which ensured that they were in the tetragonal form and not near the morphotropic-phase boundary (MPB). This is in contrast to 8/65/35 PLZT which is at a tetragonal-rhombohedral morphotropic boundary.

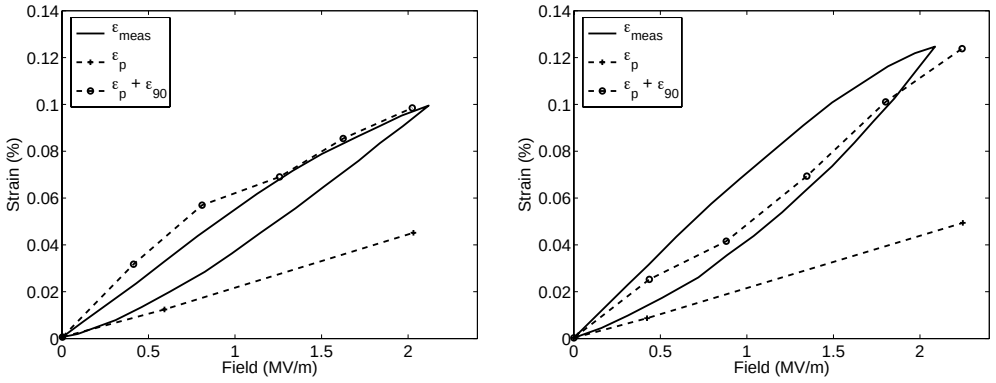

Figure 14: Measured strains ε_{meas}, strains $\varepsilon_p = d_{33}E$ due to linear piezoelectric effects, and strains $\varepsilon_p + \varepsilon_{90}$ due to piezoelectric effects and 90^o dipole rotation for (a) PZT and (b) PL8ZT data from [84].

Biased minor strain loops for PZT and PL8ZT data from [84] are shown in Figure 14 and the P-E hysteresis curve and E-ε butterfly curve for PL8ZT are plotted in Figure 15. In each case, ε_{meas} is the measured strain, $\varepsilon_p = d_{33}E$ is the computed piezoelectric strain, and ε_{90} is the strain due to 90^o dipole rotation as measured using the XRD techniques. Figure 14 illustrates that piezoelectric strains contribute less than half of the measured response and that the sum of the piezoelectric and rotational effects are consistent with the measured strains. The significant contribution due to 90^o reorientation is further demonstrated for PL8ZT in Figure 15. Here it is observed that 90^o reorientation constitutes a primary strain contribution at fields below the coercive field.

These results demonstrate that 90^o reorientation is one of the primary strain producing mechanisms in polycrystalline materials, especially at low field levels. Hence it must be incorporated in models to achieve accurate material characterization.

Furthermore, Li et al. [54] demonstrate using XRD analysis that polarization switching in PZT compounds, with compositions near the morphotropic boundary, are due primarily to two successive 90^o switches rather than a single 180^o transition. It is further noted in [96] that 180^o switching occurs more rapidly than 90^o switching as exemplified for $BaTiO_3$ by the nearly flat P-ε region in Figure 11(c). Hence we model 180^o switches with a different timescale than the 90^o rotations that produce large changes in strains.

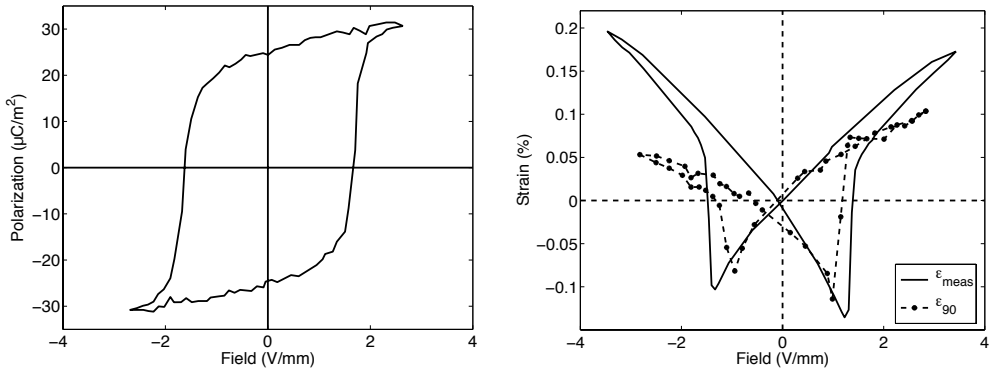

Figure 15: (a) E-P PL8ZT data from [84]. (b) Total field-induced strains ε_{meas} and strains ε_{90} due to 90^o dipole rotation for PL8ZT data from [84].

Rhombohedral PLZT

The PLZT compound 8/65/35 differs from the previously described PL8ZT material in that it has a rhombohedral rather than tetragonal crystal structure. Hence polarization switches of 70.5^o (three nearest corners) or 109.5^o (three further corners) produce deformations or strains in the material [9, 61]. Like PMN, it is also a relaxor ferroelectric material.

It is illustrated in Figure 11(g)-(i) that the D-ε behavior of 8/65/35 PLZT is quadratic and nearly anhysteretic whereas the E-ε curve has the usual hysteretic butterfly shape. In [94], these effects were modeled as electrostrictive strains. However, they are more likely due to domain switching for the previously mentioned reasons.

There are various options to model the quadratic strain behavior. One is to construct energy functionals having quadratic polarization or D-field dependence [69]. This models the quadratic P-ε or D-ε behavior in a phenomenological sense. A second alternative is to employ energy relations that incorporate the dipole switching mechanisms in combination with linear constitutive relations. This is the strategy that we employ in Section 3 and 4.

3 Homogenized Energy Model — Polarization

The homogenized energy model (HEM) for ferroelectric materials is a multiscale approach comprised of two fundamental components: (i) construction of energy-based grain-level kernels that characterize dipole switching, material constitutive behavior, and thermal relaxation mechanisms, and (ii) construction of macroscale models through the assumption that coercive fields, critical driving forces, and interaction fields are manifestations of underlying densities rather than constants.

Ferroelectric materials subjected to general fields $\vec{E} = [E_1, E_2, E_3]$ or stresses $\vec{\sigma}$ exhibit vector-valued polarization $\vec{P} = [P_1, P_2, P_3]$ polarization or strain $\vec{\varepsilon}$ responses. As illustrated in Section 1, however, many actuators and sensors employ 1-D input and output responses so, for these applications, it is advantageous to consider scalar electric and mechanical variables $E = E_3, \sigma = \sigma_{33}, P = P_3$ and $\varepsilon = \varepsilon_{33}$. For applications that require truly 2-D or 3-D polarization or strain relations, energy functionals can be constructed using the framework in [46, 47].

We summarize first the homogenized energy model for polarization. As illustrated in Figure 7, the primary polarization features for small force regimes can be defined by considering only $\pm 180^o$ dipole states. Whereas this case has been previously reported in [75, 78–80], the summary provided here motivates and provides the context for the strain-polarization model in Section 4. Moreover, we present new theory in Section 3.2 for the transition likelihoods.

3.1 Polarization Kernels with Negligible Thermal Activation

To characterize 180^o dipole switching, we employ the Gibbs energy density[1]

$$G(E,P) = \psi(P) - EP = \begin{cases} G_-(E,p) = \frac{1}{2}\eta(P+P_R)^2 - EP & , \ P \le -P_I \\ G_+(E,P) = \frac{1}{2}\eta(P-P_R)^2 - EP & , \ P \ge P_I \\ G_u(E,P) = \frac{1}{2}\eta(P_I - P_R)\left(\frac{P^2}{P_I} - P_R\right) - EP & , \ |P| < P_I \end{cases} \tag{6}$$

[1]The fact that G is an energy density results from the polarization definition $\vec{P} = \lim_{dV\to 0}\left[\frac{1}{dV}\sum_{i=1}^{N_V dV}\vec{p}_i\right]$ where $\vec{p}_i$ is a collection of general dipoles in a nonhomogeneous region, dV is a reference volume and N_V denotes the number of dipoles per unit volume [6]. The polarization thus designates the dipole moment density of the material and has units of coulombs per square meter ($\mathrm{C/m^2}$). This motivates some authors to use the terminology "polarization density" or "dipole moment density" when introducing the polarization [23, 26].

where ψ is a piecewise quadratic Helmholtz energy and P_R, η and P_I respectively denote the remanence polarization, inverse susceptibility after switching, and the positive inflection point.[2]

For regimes in which thermal excitation is negligible, the condition $\frac{\partial G}{\partial P} = 0$, which reflects the reorientation of dipoles to achieve energy minimization, yields the linear local polarization relations

$$P_m^-(E) = \frac{E}{\eta} - P_R \ , \ P_m^+(E) = \frac{E}{\eta} + P_R \ , \ P_M(E) = \frac{P_I E}{\eta(P_I - P_R)}. \tag{7}$$

The Gibbs energy density corresponding to these two equilibrium conditions is

$$G_\alpha(E) = -\frac{1}{2}\chi E^2 - E P_R^\alpha \tag{8}$$

where $\alpha = \pm 180$ and $\chi = \frac{1}{\eta}$.

To specify a hysteresis kernel, or hysteron, we consider an ideal lattice with volume V having N cells of the form depicted in Figure 6(a). We let N_- and N_+ denote the number of negatively and positively oriented dipoles so the corresponding dipole fractions are $x_+ = \frac{N_+}{N}$, $x_- = \frac{N_-}{N}$. Because $N_+ + N_- = 1$, it follows immediately that

$$x_+ + x_- = 1. \tag{9}$$

We let P^-, P^+ denote the polarizations due to negative and positive dipoles and let $p_{\alpha\beta}, \alpha, \beta = \pm 180$, which has units of (1/s), denote the likelihood of transitioning form an α-well to β-well.

The evolution of dipole fractions is governed by the differential equation

$$\begin{aligned} \dot{x}_+ &= -p_{+-}x_+ + p_{-+}x_- \\ \dot{x}_- &= p_{+-}x_+ - p_{-+}x_- \end{aligned}$$

which can be simplified to

$$\dot{x}_+ = -p_{+-}x_+ + p_{-+}(1 - x_+) \tag{10}$$

using the identity (9). The hysteron is given by

$$\overline{P} = x_+ P^+ + x_- P^-. \tag{11}$$

The specification of p_{-+}, p_{+-}, P^+, P^- depends on the degree to which kinetics due to thermal activation are relevant. For operating conditions in which relaxation due to thermal activation is negligible, it is shown in [75] that transition likelihood rates are given by

$$p_{-+} = \begin{cases} \frac{1}{\tau} & , \quad E > E_c \\ 0 & , \quad \text{else} \end{cases} \quad , \quad p_{+-} = \begin{cases} \frac{1}{\tau} & , \quad E < -E_c \\ 0 & , \quad \text{else} \end{cases} \tag{12}$$

where $1/\tau$ is the frequency at which dipoles attempt to switch. As illustrated in Figure 7, E_c denotes the coercive field which is related to P_I and P_R via the expression $E_c = \eta(P_R - P_I)$. For this operating regime, $P^+ = P_m^+$ and $P^- = P_m^-$ so the hysteron is

$$\overline{P} = \frac{E}{\eta} - P_R + 2x_+ P_R. \tag{13}$$

To incorporate the kinetics due to thermal activation, which produces creep and accommodation or reptation-like effects, likelihoods can be specified in terms of two quantities: error functions resulting from the theory of thermally activated processes or activation energies ΔG_a.

[2]We employ (6) to collectively specify the Gibbs energy density for both the positive and negative polarization variants. Because the global expression (6) is bistable, it is not a Gibbs energy density in the classical sense which has prompted some authors to designate it a Landau energy [10, 25]. Because, we are not employing higher-order polynomials, as is typically the case for the Landau energy, we follow the precedent set by authors such as Devonshire [22] who use this global representation with the understanding that its reversible Legendre transform properties hold for the individual variants.

3.2 Theory of Thermally Activated Processes

We illustrate the theory in the context of determining the likelihood that a dipole switches from negative to positive. If we sum over the index set of negative dipoles, the resulting polarization is

$$P^- = \frac{1}{V}\sum_{i=1}^{N_-} N_i p_i.$$

However, for the purpose of energy formulation and minimization, it is advantageous to sum over the set of possible states rather than the index set For a finite set of negative dipole states S_-, this yields the relations

$$N_- = \sum_{p\in S_-} N_p \quad , \quad P^- = \frac{1}{V}\sum_{p\in S_-} pN_p \tag{14}$$

where N_p is a distribution quantifying the number of dipoles having strength p as illustrated in Figure 16(b). For a continuum of dipole values, N_- and P^- are given by

$$N_- = \int_{p\in S_-} N(p)dp \quad , \quad P^- = \frac{1}{V}\int_{p\in S_-} pN(p)dp. \tag{15}$$

We consider first the case when S_- is finite.

The Gibbs energy for negatively oriented dipoles is

$$g = \Phi + K - ST - E\mathcal{P}^-$$

where Φ and K denote the internal and kinetic energies, S is the entropy, T is temperature in degrees Kelvin, and $\mathcal{P}^-$ is the total dipole strength. We note that g has units of V·C and hence it is an energy rather than an energy density like G given in (6). The internal energy is taken to be

$$\Phi = \sum_{p\in S_-} \phi(p)N_p$$

where $\phi(p)$ quantifies the internal energy for each dipole of strength p. Letting p_0 denote the spontaneous strength of a negatively oriented dipole, an appropriate choice for $\phi(p)$ is

$$\phi(p) = \frac{1}{2}\eta(p+p_0)^2 + \eta_1.$$

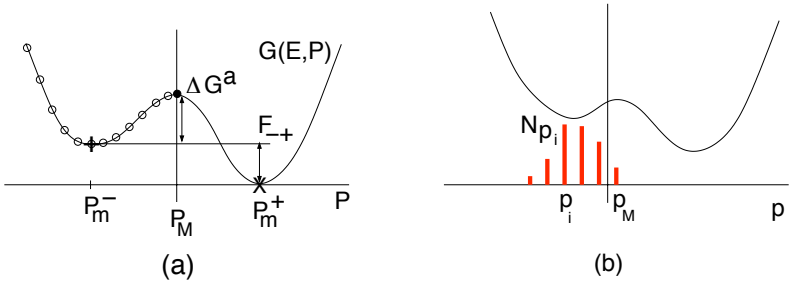

Figure 16: (a) Dipole configurations used to construct p_{-+} using the theory of thermally activated processes (ooo•), the activation energy ΔG^a $(+,\bullet)$ and the thermodynamic driving force F_{-+} $(+,x)$. (b) Negative dipole states p and density N_p.

Following [72], where analogous arguments are presented for SMA, we assume that K is a linear function of temperature and take

$$K = A(T - T_R)$$

where T_R is the reference temperature where the internal energy satisfies $U_R = 0$. This is analogous to the molecular kinetic energy relation $K = \frac{1}{2}kT$.

To compute the entropy, we note that

$$W = \frac{N_-!}{\prod_{p\in S_-} N_p!}$$

quantifies the number of ways to arrange N_- dipoles so that their states p have the distribution N_p. Boltzmann's law,

$$S = k \ln W,$$

then quantifies the entropy which can be approximated by

$$S = kN_- \ln N_- - k \sum_{p\in S_-} N_p \ln N_p$$

using Stirling's formula $\ln x! \approx x \ln x - x$. Finally, we let

$$\mathcal{P}^- = \sum_{p\in S_-} pN_p$$

denote the total dipole strength. Note that $\mathcal{P}^-$ differs from the polarization P^- in the sense that the latter reflects the dipole strength per unit volume which renders it a density; compare with (7) or (15).

The kinetics of dipole motion are governed by a partial equilibrium of the internal, kinetic, entropic and electrostatic energies subject to the constraint $N_- = \sum_{p\in S_-} N_p$. To reformulate this as an unconstrained optimization problem, we employed the augmented Gibbs functional

$$\begin{aligned} g_\gamma &= g + \gamma\left(N_- - \sum_{p\in S_-} N_p\right) \\ &= \sum_{p\in S_-} \left[\phi(p) + kT \ln N_p - Ep\right] N_p + A(T - T_R) - kTN_- \ln N_- + \gamma\left(N_- - \sum_{p\in S_-} N_p\right) \end{aligned}$$

where γ is a Lagrange multiplier. For a fixed set of dipole states, the distribution N_p is determined by the equilibrium condition $\delta g_\gamma = 0$ where δg_γ is the first variation with respect to N_p. Under the assumption that for a given state p, N_p is sufficiently large to permit consideration of the derivative $\frac{\partial g_\gamma}{\partial N_p}$, this yields

$$N_p = \exp\left(\frac{\gamma}{kT} - 1\right) \exp\left[-\left(\frac{\phi(p) - Ep}{kT}\right)\right].$$

From (14), it follows that

$$\frac{N_p}{N_-} = \frac{\exp\left[-\left(\frac{\phi(p)-Ep}{kT}\right)\right]}{\sum_{p\in S_-} \exp\left[-\left(\frac{\phi(p)-Ep}{kT}\right)\right]}. \tag{16}$$

We note that (16) quantifies the probability of observing N_p dipoles for each dipole state p as illustrated in Figure 16(b). It can also be interpreted as the probability that a dipole p, subjected to a field E, has an energy level

$$\tilde{g}(E, p) = \phi(p) - Ep; \tag{17}$$

that is

$$\mu(\tilde{g}) = \frac{\exp\left[-\tilde{g}(E,p)/kT\right]}{\sum_{p\in S_-}\exp\left[-\tilde{g}(E,p)/kT\right]}. \tag{18}$$

The likelihood rate p_{-+} that a dipole has the energy to switch from negative to positive is thus

$$p_{-+} = \frac{1}{\tau}\frac{\exp\left[-\tilde{g}(E,p_M)/kT\right]}{\sum_{p\in S_-}\exp\left[-\tilde{g}(E,p)/kT\right]} \tag{19}$$

where p_M is the dipole strength of the unstable equilibrium as shown in Figure 16(b). Note that $1/\tau$ is the frequency at which dipoles attempt to switch so $1/\tau$ has units of 1/s.

Polarization Model Likelihoods

To construct the likelihood rates p_{-+} and p_{+-} for the polarization model, we recall that the polarization is the dipole density which has units of $\mathrm{C/m^2}$. We employ the energy density G given by (6) which corresponds to the dipole energy (17). Furthermore, we consider a continuum of dipole strengths and approximate sums by integrals. Finally, we approximate evaluation at the unstable equilibrium P_M by evaluation at the inflection points $-P_I$ or P_I.

These approximations yield the expressions

$$\mu(G) = Ce^{-GV/kT} \tag{20}$$

and

$$p_{+-} = \frac{1}{\tau}\frac{e^{-G(E,P_I)V/kT}}{\displaystyle\int_{P_I}^{\infty} e^{-G(E,P)V/kT}dP} = \frac{\gamma_1}{\mathrm{erfcx}(E_p(t))}\ ,\ p_{-+} = \frac{1}{\tau}\frac{e^{-G(E,-P_I)V/kT}}{\displaystyle\int_{-\infty}^{-P_I} e^{-G(E,P)V/kT}dP} = \frac{\gamma_1}{\mathrm{erfcx}(E_n(t))} \tag{21}$$

for the Boltzmann transition probability[3] and transition likelihood rates.[4] Here erfcx denotes the complementary error function. As detailed in [13],

$$E_n(t) = \gamma_2(E(t) - E_c) \quad , \quad E_p(t) = \gamma_2(-E(t) - E_c),$$

and

$$\gamma_1 = \frac{1}{\tau}\sqrt{\frac{2V\eta}{\pi kT}} = \frac{1}{\beta\tau}\sqrt{\frac{2}{\pi}} \quad , \quad \gamma_2 = \sqrt{\frac{V}{2kT\eta}} = \frac{1}{\beta\eta\sqrt{2}} \quad , \quad \beta = \sqrt{\frac{kT}{\eta V}}.$$

Activation Energies $\boldsymbol{\Delta G^a}$

Use of the theory of thermally activated processes to construct transition likelihoods has the advantage that it can be directly motivated by fundamental thermodynamics concepts. However, its efficiency diminishes when additionally quantifying 90^o switching or 2-D or 3-D polarizations

[3]The inclusion of the reference volume V in the expressions (20) and (21) is due do the definition of polarization as the dipole density and G as an energy density — compare with the dipole relations (18) and (19). For some applications, the estimation of parameters yields values of V that correspond to domain or grain dimensions. In general, however, it is simply the reference volume in the definition of P.

[4]Because probabilities for continuous densities are defined in terms of integrals, the probability of measuring a discrete point is zero. Hence one must use care when interpreting the relations (20) and (21). The point evaluations are associated with the discrete set of polarization states with sums approximated by integrals to permit formulation in terms of error functions. The proportionality factor associated with converting sums to integrals is incorporated in the term $\frac{1}{\tau}$. An alternative interpretation for continuous densities is provided in [75].

due to the higher degree of energy landscapes and difficulty evaluating integrals based on inflection lines. This motivates consideration of an alternative formulation based on activation energies ΔG^a as proposed in [47, 92].

As illustrated in Figure 16, the activation energy is the difference between stable and unstable equilibria. For switching between the negative and positive well, we employ the formulation

$$\begin{aligned}\Delta G^a_{-+}(E) &= \begin{cases} G_u(E,P_M) - G_-(E,P_m^-) & , \quad -E_c \le E \le E_c \\ G_u(-E_c,P_M) - G_-(-E_c,P_m^-) & , \quad E < -E_c \\ 0 & , \quad E > E_c \end{cases} \\ &\approx \begin{cases} \frac{1}{2}\frac{P_R}{E_c}(E-E_c)^2 & , \quad E \le E_c \\ 0 & , \quad E > E_c \end{cases}\end{aligned}$$

where G_u, G_- are defined in (6) and P_m^-, P_m are defined in (7). As illustrated in Figure 16, the unstable equilibrium exists only for $-E_c \le E \le E_c$. For computational purposes, we employ the limiting values for $E > E_c$ and $E < -E_c$. This differs from the linear formulation employed in [47] but yields the same computational value for the transition likelihoods.

For the polarization model based on positive and negative switching, it is easy to specify the unstable component $G_u(E,P)$ which provides a continuously differentiable transition between the stable negative and positive equilibrium states. For 2-D and 3-D polarization models or models that incorporate 90^o switching behavior, it is difficult to construct continuously differentiable, or even simply continuous, transitions in landscapes between the regions of local minima. This is the same problem that plagues the construction of multi-dimensional splines. Moreover, it is unnecessary since the transition regions represent unstable dipole behavior. An alternative is to formulate transition likelihoods based on thermodynamic driving forces.

For this regime, the thermodynamic driving force is defined to be

$$\begin{aligned}F_{-+}(E) &\equiv G_-(E) - G_+(E) = 2EP_R \\ F_{+-}(E) &\equiv G_+(E) - G_-(E) = -2EP_R\end{aligned}$$

(see [9] and included references). If we define the critical driving force to be

$$F_c = 2E_cP_R, \tag{22}$$

then the activation energy can be expressed as

$$\Delta G^a_{-+}(E) = \begin{cases} \Delta G_0\left(1 - F_{-+}(E)/F_c\right)^2 & , \quad F_{-+}(E) \le F_c \\ 0 & , \quad F > F_c \end{cases}$$

where $\Delta G_0 \equiv F_c/4$ denotes the value of the energy barrier at zero driving force. The definition of ΔG^a_{+-} is analogous. We note that in the homogenized energy model, F_c, and hence ΔG_0, is treated as a material parameter whose values are realizations of an underlying density.

The likelihood relations

$$p_{-+}(E) = \frac{1}{\tau}e^{-\Delta G^a_{-+}(E)V/kT} \quad , \quad p_{+-}(E) = \frac{1}{\tau}e^{-\Delta G^a_{+-}(E)V/kT} \tag{23}$$

follow directly from the previous Boltzmann theory when we consider only polarization values P_m^-, P_m^+ and P_M. This formulation facilitates implementation by eliminating integration over complex regions but it neglects the geometry of the energy surface in regions near minima since it is equivalent to summing or integrating over square energy wells. In addition to being used in [47], the activation energy is employed in [4] to construct Debye relations for ferroelectric materials. It is also used in [10] for constructing magnetic models and [20] where analogous models are developed for SMA.

3.3 Polarization Kernel that Incorporates Thermal Relaxation

Solution of the differential equation (10) using the likelihood relations (21) or (23) quantifies the dipole fraction x_+ and $x_- = 1 - x_+$. The general polarization hysteron is then given by (11).

As detailed in [75, 78–80], P^- and P^+ for the thermally active case are given by

$$P^+(E) = \int_{P_I}^{\infty} P\mu(G(E,P)dP \quad , \quad P^-(E) = \int_{-\infty}^{-P_I} P\mu(G(E,P)dP \tag{24}$$

where μ is defined in (20). For the likelihood relations (21), it is shown in [13] that the kernel can be expressed as

$$\overline{P}(E;E_c) = \frac{E}{\eta} - P_R + 2x_+P_R + \tilde{P}(E)$$

where $\tilde{P}(E;E_c) = \gamma_4\,(x_+ - 1)\,p_{-+} + p_{+-}x_+$ and $\gamma_4 = \frac{\tau kT}{\eta V}$. To determine the limiting behavior of $\tilde{P}$, we note that when p_{-+} is large and hence p_{+-} is small, the likelihood that dipoles are positive is large which implies that $x_+ \approx 1$. Similarly, p_{-+} small and p_{+-} large yields $x_+ \approx 0$. Finally, $\overline{P}(0) = -\gamma_4$ where γ_4 is typically on the order of 10^{-6} to 10^{-8} for ferroelectric materials. The approximation $\tilde{P}(E) = 0$ then yields the kernel expression

$$\overline{P}(E,E_c) = \frac{E}{\eta} - P_R + 2x_+P_R \tag{25}$$

which is the negligible thermal activation relation (13). Alternatively, it is shown in Section 2.6.3 of [75] that use of Dirac sequences yields (25) as an appropriate low thermal activation limit.

3.4 Homogenized Energy Model

To incorporate the effects of polycrystallinity, material nonhomogeneities, and variable interaction fields, we assume that interaction fields E_I and certain material coefficients are manifestations of underlying densities rather than constants. It is illustrated in [13,75,78,80] that the assumption that coercive fields are distributed yields a $\pm 180^o$ switching polarization model

$$\begin{aligned} P(E(t);x_+^0) &= \int_0^{\infty}\int_{-\infty}^{\infty} \overline{P}(E(t)+E_I;E_c)\nu_I(E_I)\nu_c(E_c)dE_IdE_c \\ &= \frac{E}{\eta} - P_R + 2P_R\int_0^{\infty}\int_{-\infty}^{\infty} x_+(E_e(t);E_c)\nu_I(E_I)\nu_c(E_c)dE_IdE_c, \end{aligned} \tag{26}$$

that accurately quantifies polycrystalline behavior. Here

$$E_e(t) \equiv E(t) + E_I \tag{27}$$

is the effective electric field, x_+^0 is the initial fraction of positively oriented dipoles, and ν_c and ν_I are densities associated with the coercive and interaction fields which satisfy the constraints

$$\begin{aligned} &\text{(i)} \quad \nu_c(E_c) \ \text{ defined for } \ E_c > 0, \\ &\text{(ii)} \quad \nu_I(-E_I) = \nu_I(E_I), \\ &\text{(iii)} \quad |\nu_c(E_c)| \le c_1e^{-a_1E_c} \quad , \quad |\nu_I(E_I)| \le c_2e^{-a_2|E_I|} \end{aligned} \tag{28}$$

for positive constants c_1, a_1, c_2, a_2. These assumptions enforce the physical properties that local coercive fields are positive, low-field Rayleigh loops are symmetric, and local coercive and interaction fields decay as a function of distance. Details regarding density construction are provided in Section 4.2.2 and quadrature rules to approximate the integrals in (26) are provided in Section 4.3.

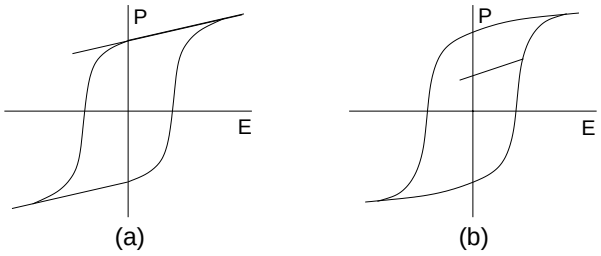

Figure 17: Hysteresis behavior when (a) ν_c is distributed but ν_I is constant, and (b) ν_I is distributed but ν_c is constant.

The necessity of considering densities for both E_I and E_c is illustrated in Figure 17 by illustrating the hysteresis behavior that results if either is neglected. As shown in Figure 17(a), the assumption that ν_c is distributed but ν_I is constant yields loops which exhibit no switching as fields are reduced until the value $E = 0$ with similar behavior for increasing fields. As illustrated in Figure 11(d)-(f) for PZT, this is not the case for ferroelectric materials. The assumption that ν_c is constant and ν_I distributed yields the minor loop behavior depicted in Figure 17(b). Due to the symmetry of ν_I, this forces minor loops to be rotationally symmetric about $E = 0$ which is not the behavior exhibited by materials. This necessitates the inclusion of both densities.

4 Homogenized Energy Model — Strain and Polarization

To quantify the strain and polarization behavior detailed in Section 2 for various stress regimes, it is necessary to additionally incorporate 90^o switching. As motivated by common actuator geometries and to simplify the discussion, we still focus on 1-D input and output responses. For tetragonal materials, the projection of $\vec{P}$ in Figure 6 onto the 3-axis yields spontaneous polarization variants or states at $\pm 180^o, 90^o$ which are respectively designated $P_0^\alpha, \alpha = \pm, 90$. Similarly rhombohedral materials, such as PLZT, have variants at $\pm 180^o, 70.5^o$ and 109.5^o.

We note that the construction of grain-level or single crystal polarization and strain kernels follows the development in [47, 92]. However, these authors do not consider the homogenized energy framework, developed in Section 4.2, which is necessary to characterize polycrystalline materials.

4.1 Strain and Polarization Kernels

For $\alpha = \pm 180, 90$, the Helmholtz and Gibbs energy densities for the α-well are

$$\psi_\alpha(P, \varepsilon) = \frac{1}{2}\eta_\alpha^\varepsilon (P - P_R^\alpha)^2 + \frac{1}{2} Y_\alpha^P (\varepsilon - \varepsilon_R^\alpha)^2 + h_\alpha (P - P_R^\alpha)(\varepsilon - \varepsilon_R^\alpha) \tag{29}$$

and

$$G_\alpha(E, \sigma; P, \varepsilon) = \psi_\alpha(P, \varepsilon) - EP - \sigma\varepsilon. \tag{30}$$

As summarized in the nomenclature table at the beginning of the paper, P_R^α and ε_R^α are the remanent polarization and strain of the α-variant. The parameters $\eta_\alpha^\varepsilon, Y_\alpha^P$ and h_α are the inverse susceptibility at constant strain, elastic stiffness at constant polarization, and piezoelectric constant, respectively.

For a fixed applied stress σ and field E, the conditions

$$\frac{\partial G}{\partial P} = 0 \ , \ \frac{\partial G}{\partial \varepsilon} = 0$$

can be used to determine pairs $(P_m^\alpha, \varepsilon_m^\alpha)$ that minimize the Gibbs energy. Specifically, this yields

$$\begin{aligned} E &= \eta_\alpha^\varepsilon (P_m^\alpha - P_R^\alpha) + h_\alpha (\varepsilon_m^\alpha - \varepsilon_R^\alpha) \\ \sigma &= Y_\alpha^P (\varepsilon_m^\alpha - \varepsilon_R^\alpha) + h_\alpha (P_m^\alpha - P_R^\alpha) \end{aligned}$$

which can be inverted to obtain

$$\begin{aligned} P_m^\alpha &= P_R^\alpha + \chi_\alpha^\sigma E + d_\alpha \sigma \\ \varepsilon_m^\alpha &= \varepsilon_R^\alpha + d_\alpha E + s_\alpha^E \sigma \end{aligned} \tag{31}$$

where

$$\chi_\alpha^\sigma = \frac{Y_\alpha^P}{Y_\alpha^P \eta_\alpha^\varepsilon - h_\alpha^2} \ , \ d_\alpha = \frac{h_\alpha}{h_\alpha^2 - Y_\alpha^P \eta_\alpha^\varepsilon} \ , \ s_\alpha^E = \frac{\eta_\alpha^\varepsilon}{Y_\alpha^P \eta_\alpha^\varepsilon - h_\alpha^2}.$$

Note that (31) provides the linear domain-level constitutive equations shown in Figure 4. The minimum of the Gibbs energy density in each α-well can thus be expressed as

$$G_{\alpha m}(E, \sigma) = -\frac{1}{2}\chi_\alpha^\sigma E^2 - \frac{1}{2} s_\alpha^E \sigma^2 - d_\alpha E \sigma - E P_R^\alpha - \sigma \varepsilon_R^\alpha. \tag{32}$$

We note that within each well, the Gibbs energy density (32) is the negative Legendre transform of the Helmholtz energy density (29).

To construct the activation energies employed in transition likelihoods, we note that the thermodynamic driving forces required to transition from an α-well to β-well can be expressed as

$$\begin{aligned} F_{\alpha\beta}(E, \sigma) &= G_{\alpha m}(E, \sigma) - G_{\beta m}(E, \sigma) \\ &= \tfrac{1}{2}\Delta\chi_{\alpha\beta}^\sigma E^2 - \tfrac{1}{2}\Delta s_{\alpha\beta}^E \sigma^2 - \Delta d_{\alpha\beta} E\sigma - E\Delta P_R^{\alpha\beta} - \sigma \Delta \varepsilon_R^{\alpha\beta} \end{aligned}$$

where

$$\begin{gathered} \Delta\chi_{\alpha\beta}^\sigma = \chi_\alpha^\sigma - \chi_\beta^\sigma \ , \ \Delta s_{\alpha\beta}^E = s_\alpha^E - s_\beta^E \ , \ \Delta d_{\alpha\beta} = d_\alpha - d_\beta \\ \Delta P_R^{\alpha\beta} = P_R^\alpha - P_R^\beta \ , \ \Delta \varepsilon_R^{\alpha\beta} = \varepsilon_R^\alpha - \varepsilon_R^\beta. \end{gathered}$$

Based on the assumption that dipoles are restricted to three orientations $\alpha = \pm, 90$, we let x_+, x_- and x_{90} denote the dipole fractions associated with negatively, positively, and 90^o-oriented dipoles. The evolution of dipole fractions is governed by the differential equation

$$\begin{aligned} \dot{x}_- &= -(p_{-90} + p_{-+})x_- + p_{90-}x_{90} + p_{+-}x_+ \\ \dot{x}_{90} &= p_{-90}x_- - (p_{90-} + p_{90+})x_{90} + p_{+90}x_+ \\ \dot{x}_+ &= p_{-+}x_- + p_{90+}x_{90} - (p_{+90} + p_{+-})x_+ \end{aligned}$$

which can be simplified to

$$\begin{aligned} \dot{x}_- &= -(p_{-90} + p_{-+} + p_{90-})x_- + (p_{+-} - p_{90-})x_+ + p_{90-} \\ \dot{x}_+ &= (p_{-+} - p_{90+})x_- - (p_{+90} + p_{+-} + p_{90+})x_+ + p_{90+} \end{aligned} \tag{33}$$

using the identity $x_+ + x_- + x_{90} = 1$.

As motivated by the discussion in Section 3.1, the likelihood rates $p_{\alpha\beta}$ of transitioning from an α-well to β-well are specified by

$$p_{\alpha\beta}(E, \sigma) = \frac{1}{\tau_{\alpha\beta}} e^{-\Delta G_{\alpha\beta}^a(E,\sigma)V/kT}. \tag{34}$$

The activation energy is specified by the relation

$$\Delta G^a_{\alpha\beta}(E,\sigma;F_c) = \begin{cases} \Delta G_0(1-F_{\alpha\beta}(E,\sigma)/F_c)^2 & , \ F_{\alpha\beta}(E,\sigma) \le F_c \\ 0 & , \ F_{\alpha\beta}(E,\sigma) > F_c \end{cases} , \ \Delta G_0 = \begin{cases} \frac{1}{4}F_c \ , \ 180^o \text{ Switching} \\ \frac{1}{16}F_c \ , \ 90^o \text{ Switching} \end{cases}$$

where ΔG_0 is the energy barrier at zero driving force. We note that the critical driving force F_c is assumed to be a manifestation of an underlying density in the homogenized energy model.

It is noted in Section 2.2 and [47,96] that whereas 180^o switchings is often comprised of successive 90^o switches, it typically occurs on a faster timescale than strain-producing 90^o switches. These different timescales are accommodated by the inclusion of 180^o likelihood rates p_{-+}, p_{+-} and use of different relaxation times $\tau_{\alpha,\beta}$ for 90^o and 180^o switchings.

The polarization and strain kernels are given by

$$\overline{P} = \sum_{\alpha=\pm,90} x_\alpha P^\alpha \quad , \quad \overline{\varepsilon} = \sum_{\alpha=\pm,90} x_\alpha \varepsilon^\alpha$$

where

$$P^\alpha = \int_\alpha P\mu(P,\varepsilon)dPd\varepsilon \quad , \quad \varepsilon^\alpha = \int_\alpha \varepsilon\mu(P,\varepsilon)dPd\varepsilon \tag{35}$$

are the polarization and strain associated with each well. In (35), integration is performed over a region of the energy minima and $\mu(P^\alpha,\varepsilon^\alpha)$ given by (20) quantifies the probability of finding a specific polarization and strain pair $(P^\alpha,\varepsilon^\alpha)$.

The evaluation of the integrals (35) is difficult for higher-dimensional energy landscapes which significantly diminishes implementation speeds. To address this, we employ the low thermal activation approximations discussed in Section 3.2 and employ the approximations $P^\alpha = P^\alpha_m, \varepsilon^\alpha = \varepsilon^\alpha_m$ where $P^\alpha_m, \varepsilon^\alpha_m$ are given in (31). The kernels are subsequently given by[5]

$$\overline{P} = \sum_{\alpha=\pm,90} x_\alpha P^\alpha_m \ , \ \overline{\varepsilon} = \sum_{\alpha=\pm,90} x_\alpha \varepsilon^\alpha_m. \tag{36}$$

To construct a form of the kernel that facilitates comparison with existing models posed in terms of reversible and irreversible components and construction of constitutive models for coupled and distributed structures, we consider (36) in light of the assumption that

$$\begin{aligned} &\chi^\sigma_+ = \chi^\sigma_- = \chi^\sigma_{90} = \chi^\sigma \\ &s^E_+ = s^E_- = s^E_{90} = s^E \\ &P^{90}_R = 0, P^+_R = -P^-_R, \varepsilon^+_R = \varepsilon^-_R \\ &d_{90} = 0, d_- = -d_+ \\ &\tau_{90-} = \tau_{-90} = \tau_{90+} = \tau_{+90} = \tau_{90} \ , \ \tau_{-+} = \tau_{+-} = \tau_{180}. \end{aligned} \tag{37}$$

This assumption is based on the observed material behavior and does not reduce the model's generality. Substitution of (37) into (36) yields the relations

$$\begin{aligned} \overline{P}(E,\sigma) &= \bar{d}(E,\sigma)\sigma + \chi^\sigma E + \overline{P}_{irr}(E,\sigma) \\ \overline{\varepsilon}(E,\sigma) &= s^E\sigma + \bar{d}(E,\sigma)E + \overline{\varepsilon}_{irr}(E,\sigma) \end{aligned} \tag{38}$$

[5]The input and model parameters exhibit the dependencies

$$E(t), \sigma(t), x_{\pm,90}(t;E,\sigma,F_c), p_{\alpha\beta}(E,\sigma;F_c), \overline{P}(E,\sigma;F_c), \overline{\varepsilon}(E,\sigma;F_c).$$

Where the meaning is clear, we suppress certain dependencies to simplify subsequent discussion.

where

$$\begin{aligned}\overline{P}_{irr}(E,\sigma) &= \sum_{\alpha=\pm,90} P_R^\alpha x_\alpha(E,\sigma)\\ \overline{\varepsilon}_{irr}(E,\sigma) &= \sum_{\alpha=\pm,90} \varepsilon_R^\alpha x_\alpha(E,\sigma)\\ \bar{d}(E,\sigma) &= \sum_{\alpha=\pm,90} d_\alpha x_\alpha(E,\sigma)\end{aligned} \tag{39}$$

are the grain-level polarization, strain and coupling relations illustrated in Figure 4.

Example 1.

The kernel relations (39) can be used to model the behavior of certain single crystal compounds if interaction fields are negligible. This is illustrated in Figure 18 to demonstrate the ferroelastic switching behavior discussed in Section 2 and depicted in Figure 9. The parameters in Table 1 are

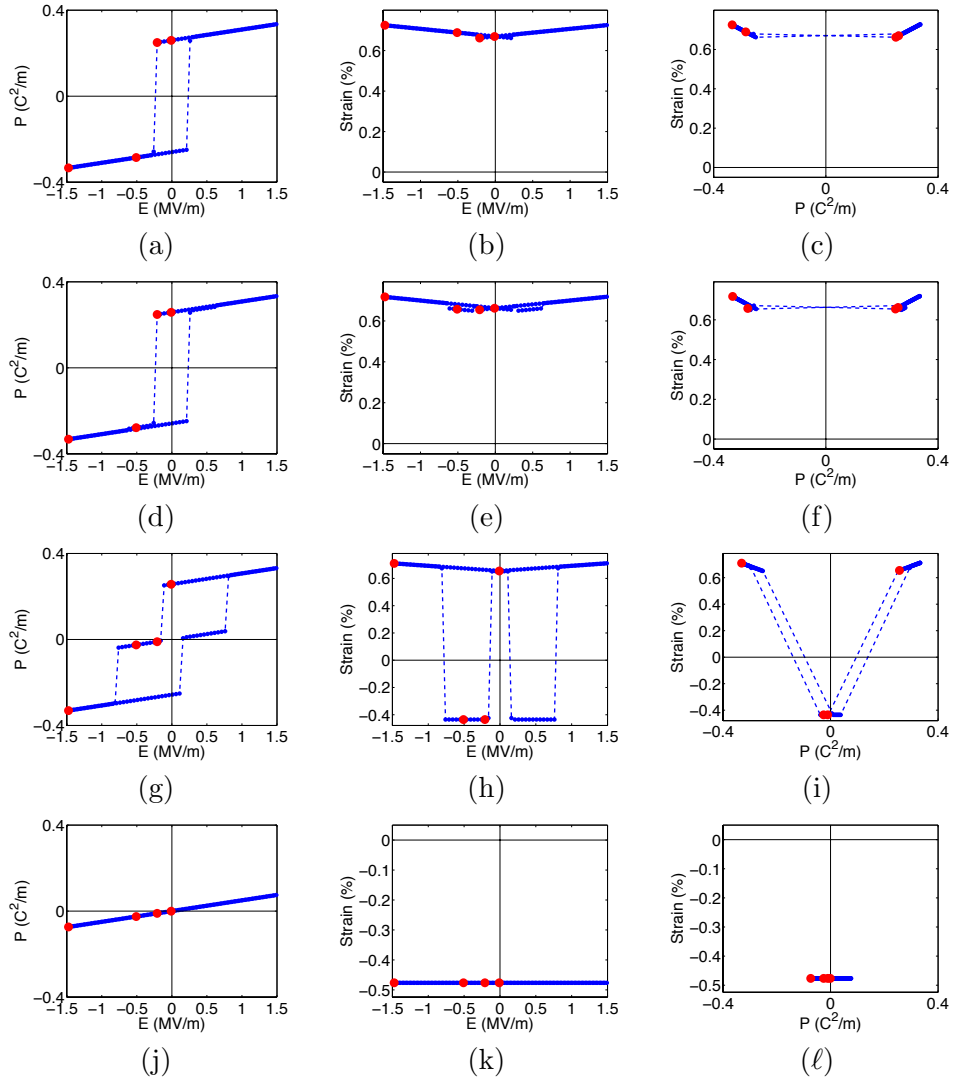

Figure 18: Simulated polarization and strain for fixed stress levels of (a)-(c) 0 MPa, (d)-(f) -4 MPa, (g)-(i) -8 MPa, and (j)-(ℓ) -30 MPa with instantaneous switching of x_α.

P_R^+	ε_R^+	ε_R^{90}	χ_+^σ	d_+	s_+^E	τ^{90}	τ_{180}
0.26	6.7×10^{-3}	-4.2×10^{-3}	5.0×10^{-8}	374×10^{-12}	18.8×10^{-12}	1.0×10^{-3}	3.0×10^{-3}

Table 1: Parameters used in the single crystal simulations.

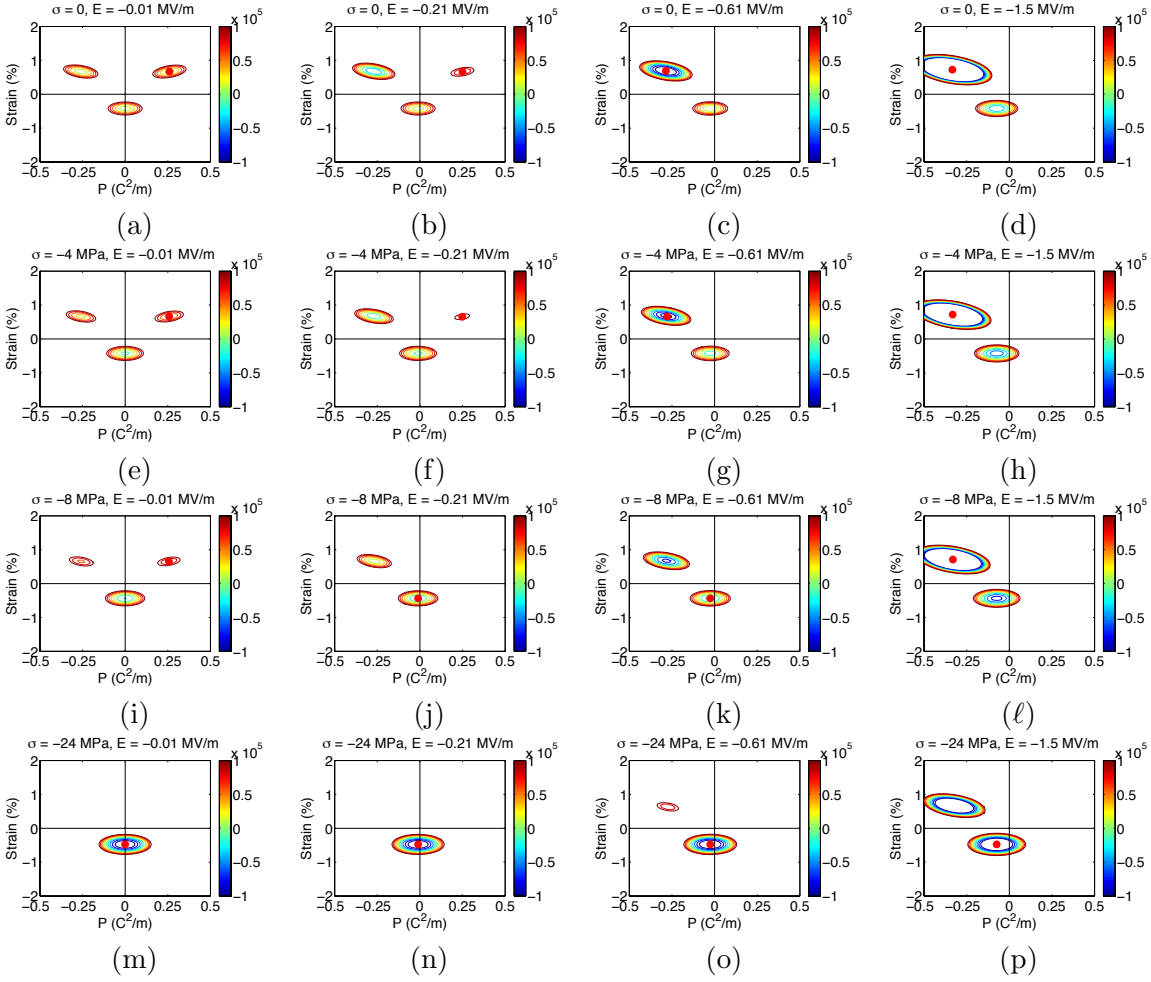

Figure 19: Gibbs energy density for fixed stress levels of (a)-(d) 0 MPa, (e)-(h) -4 MPa, (i)-(ℓ) -8 MPa, and (m)-(p) -30 MPa at the indicated input field levels.

representative of those for standard ferroelectric materials. The corresponding Gibbs energy density landscapes are plotted in Figure 19. It is observed that the application of increasing compressive prestresses shifts the landscape to favor 90^o initial orientations.

4.2 Homogenized Energy Model

As noted in Section 3.3, the effects of polycrystallinity and variable interaction fields can be incorporated by considering certain parameters to be manifestations of underlying densities. Here we employ the homogenized energy formulations

$$\begin{aligned} P(E(t),\sigma(t);x_+^0) &= \int_0^\infty \int_{-\infty}^\infty \overline{P}(E_e(t),\sigma(t);F_c)\nu_I(E_I)\nu_c(F_c)dE_I dF_c \\ \varepsilon(E(t),\sigma(t);x_+^0) &= \int_0^\infty \int_{-\infty}^\infty \overline{\varepsilon}(E_e(t),\sigma(t);F_c)\nu_I(E_I)\nu_c(F_c)dE_I dF_c \end{aligned} \tag{40}$$

where the effective field E_e is defined in (27). The choice of the critical driving force density $\nu_c(F_c)$ is motivated by its role when constructing activation energies for likelihood construction and its relation (22) to the coercive field E_c. The densities satisfy the criteria (i)–(iii) in (28) and their construction is discussed in Section 4.2.2.

With the assumption (37) and resulting kernel relations (38), (40) can be expressed as

$$\begin{aligned} P(E,\sigma) &= d(E,\sigma)\sigma + \chi^\sigma E + P_{irr}(E,\sigma) \\ \varepsilon(E,\sigma) &= s^E\sigma + d(E,\sigma)E + \varepsilon_{irr}(E,\sigma) \end{aligned} \tag{41}$$

where

$$\begin{aligned} d(E,\sigma) &= \int_0^\infty \int_{-\infty}^\infty \bar{d}(E_e;F_c)\nu_I(E_I)\nu_c(F_c)dE_I dF_c \\ P_{irr}(E,\sigma) &= \int_0^\infty \int_{-\infty}^\infty \overline{P}_{irr}(E_e;F_c)\nu_I(E_I)\nu_c(F_c)dE_I dF_c \\ \varepsilon_{irr}(E,\sigma) &= \int_0^\infty \int_{-\infty}^\infty \bar{\varepsilon}_{irr}(E_e;F_c)\nu_I(E_I)\nu_c(F_c)dE_I dF_c. \end{aligned} \tag{42}$$

We note that the terms $\chi^\sigma E$ and $s^E\sigma$ result from the fact that

$$\int_0^\infty \int_{-\infty}^\infty \nu_I(E_I)\nu_c(F_c)dE_I dF_c = 1.$$

Techniques to evaluate the integrals in (42) are detailed in Section 4.3.

We note that (41) has the form of the general constitutive relations (3) that others have derived using various micromechanical and phenomenological theories; see also Figure 4. The homogenized energy model provides the advantage of micromechanical energy analysis in combination with stochastic homogenization techniques to facilitate efficient model implementation and data-driven parameter estimation techniques [31].

4.2.1 Determination of Initial Hysteresis States

Implementation of the model (40) requires the specification of the initial dipole states. Due to the multivalued nature of hysteresis phenomena, this a shared requirement for all hysteresis models. This necessitates determining the initial state of devices with hysteretic components so it is an experimental and implementation issue in addition to being a modeling requirement.

One technique to address this is to experimentally drive devices to positive or negative saturation before the specified task to ensure an initial remanence state. To initialize the model, one can start with arbitrary initial dipole fractions; e.g., $x_+^0 = x_{90}^0 = x_-^0 = \frac{1}{3}$. Driving to positive saturation yields $x_+ = 1, x_{90}^0 = x_-^0 = 0$ and returning the field to zero yields remanence dipole fractions x_+^r, x_{90}^r and x_-^r that can be used as initial values for subsequent characterization and simulations.

4.2.2 Density Construction

A critical issue when constructing models for specific applications concerns the construction of the densities $\nu_I(E_I)$ and $\nu_c(F_c)$.[6] Here we discuss a method introduced in [24, 30] that employs the

[6] As illustrated in Figure 11, the polarization burst region and strain elbow occur at basically the same field E_c. This indicates that one value of $\bar{F}_c$ and density $\nu_c(F_c)$ can be used for both 180^o and 90^o switching processes.

expansions

$$\nu_c(F_c) = \frac{1}{c_1}\sum_{k=k_\alpha}^{K_\alpha} \alpha_k \phi_k(F_c)$$
$$\nu_I(E_I) = \frac{1}{c_2}\sum_{k=k_\beta}^{K_\beta} \beta_k \varphi_k(E_I) \tag{43}$$

where the basis functions $\phi_k(F_c)$ and $\varphi_k(E_I)$ are lognormal and normal functions and the coefficients α_k and β_k are determined through a least squares fit to data as detailed in [31].[7] The constants

$$c_1 = \sum_{k=k_\alpha}^{K_\alpha} \alpha_k \ , \ c_2 = \sum_{k=k_\beta}^{K_\beta} \beta_k$$

ensure integration to unity.

The interaction field basis functions are defined by

$$\varphi_k(E_I) = \frac{1}{\sigma_I^k\sqrt{2\pi}} e^{-E_I^2/2(\sigma_I^k)^2}$$

where the standard deviations are taken to be

$$\vec{\sigma}_I = \{\sigma_{I_k}\} = \left\{2^k \sigma_I\right\} \ , \ k = k_\alpha, \cdots, K_\alpha. \tag{44}$$

As detailed in [30, 31], data-driven techniques can be used to obtain initial values of σ_I.

Since $F_c \geq 0$, we employ lognormal functions

$$\phi_k(F_c) = \frac{1}{\sigma_c^k F_c\sqrt{2\pi}} e^{-[\ln(F_c)-\mu_c]^2/2(\sigma_c^k)^2}$$

for the driving force density. Data-driven techniques to determine $\mu_c = \ln \bar{F}_c$ are detailed in [31]. The standard deviations $\vec{\sigma}_c$ are specified in a manner analogous to (44). We note that for typical applications, reasonable accuracy can be obtained with $k_\alpha = k_\beta = -3, K_\alpha = K_\beta = 1$. Representative basis functions are plotted in Figure 20.

[7] The expansions (43) are linear with respect to the parameters α_k and β_k. This permits the use of linear least squares and linear adaptive techniques for parameter estimation and adaptation. However, these techniques are constrained by the requirement that parameters are nonnegative.

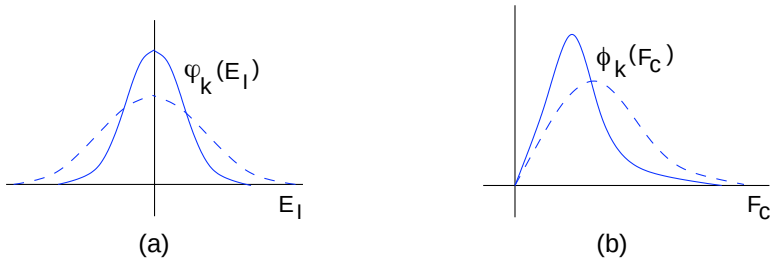

Figure 20: (a) Normal basis functions $\varphi_k(E_I)$ and (b) lognormal functions $\phi_k(F_c)$ used in the expansions (43) for $\nu_I(E_I)$ and $\nu_c(F_c)$.

4.3 Quadrature Techniques

To implement the model, the integrals defining the terms d, P_{irr} and ε_{irr} in (42) must be approximated in a manner that is both efficient and accurate. We first note that by employing the relations (39), these terms can be expressed as

$$P_{irr}(E,\sigma) = \sum_{\alpha=\pm,90} P_R^\alpha \int_0^\infty \int_{-\infty}^\infty x_\alpha(E_e;F_c)\nu_I(E_I)\nu_c(F_c)dE_I dF_c$$

$$\varepsilon_{irr}(E,\sigma) = \sum_{\alpha=\pm,90} \varepsilon_R^\alpha \int_0^\infty \int_{-\infty}^\infty x_\alpha(E_e;F_c)\nu_I(E_I)\nu_c(F_c)dE_I dF_c$$

$$d(E,\sigma) = \sum_{\alpha=\pm,90} d_\alpha \int_0^\infty \int_{-\infty}^\infty x_\alpha(E_e;F_c)\nu_I(E_I)\nu_c(F_c)dE_I dF_c$$

so the integration involves the dipole fractions in a manner analogous to (26). Secondly, the densities satisfy the exponential decay constraints (28) as shown in Figure 20. Hence approximation algorithms can be defined on finite domains rather than necessitating quadrature techniques for infinite and semi-infinite domains. We illustrate here a midpoint formula and refer the reader to [75] for details regarding composite Gaussian quadrature techniques. As detailed in [31], truncation of the domains and use of composite techniques proves more efficient to implement than Gauss-Hermite and Gauss-Laguerre algorithms, that are designed specifically for infinite and semi-infinite intervals, because they allow accurate evaluation of the density expansions (43) and construction of lookup tables to improve algorithm efficiency.

If we let F_{c_i}, E_{I_j} and v_i, w_j respectively denote the quadrature points and weights, we obtain the approximate relations

$$\int_0^\infty \int_{-\infty}^\infty x_\alpha(E+E_I;F_c)\nu_I(E_I)\nu_c(F_c)dE_I dF_c \approx \sum_{i=1}^{N_i}\sum_{j=1}^{N_j} x_\alpha(E+E_{I_j};F_{c_i})\nu_I(E_{I_j})\nu_c(F_{c_j})v_i w_j.$$

For the validation results reported in Section 6, sufficient accuracy was achieved using the trapezoid rule with $N_i = N_j = 41$.

5 Constitutive Relations for Structural Models

For isolated materials, the polarization and strain relations (40) or (41) may be suitable for characterization and simulations. However, for most applications, the ferroelectric materials are components in a system which necessitates the development of system models employing (40) or (41). Here we discuss the construction of a simple lumped model for PZT employed with a spring, damping element, and prestress and the development of constitutive equations that can be used to construct rod, beam, shell or membrane models for systems with ferroelectric actuators.

5.1 Lumped Actuator Model

We first consider a PZT actuator subjected to a prestress σ_0 and restoring spring with stiffness k as illustrated in Figure 21(a). This is representative of characterization experiments reported in [92] and can provide a simplified model for certain applications. The actuator is assumed to have length L, cross-sectional area A, and longitudinal displacements of the actuator end are denoted by $u(t)$.

For this configuration, the inputs or loads are the field E and prestress σ_0. Hence the Gibbs energy density (30) or (32) is the appropriate thermodynamic potential. The results strains are specified by (40) or (41).

The total applied force is

$$F = F_s + F_0 \tag{45}$$

where

$$F_s = -ku \ , \ F_0 = \sigma_0 A \ , \ \text{with} \ \ \sigma_0 < 0,$$

are the forces due to the restoring spring and prestress. Since $\varepsilon = \frac{u}{L}$, it follows that the applied stress is

$$\sigma = \frac{-L\varepsilon}{A}k + \sigma_0. \tag{46}$$

The substitution of (46) into (41) yields the relation

$$\varepsilon = \frac{A}{A + s^E Lk}\left[s^E\sigma_0 + d\left(E, -L\varepsilon k/A + \sigma_0\right)E + \varepsilon\left(E, -L\varepsilon k/A + \sigma_0\right)\right] \tag{47}$$

quantifying strains in terms of E and σ_0. Due to its implicit nature, solution of (47) requires a nonlinear iterative method such as a fixed-point or Newton-based algorithm.

For many applications, however, the spring stiffness k is sufficiently small that $\left|\frac{-L\varepsilon}{A}k\right| << |\sigma_0|$. For these cases, (47) can be approximated by the explicit relation

$$\varepsilon = \frac{A}{A + s^E Lk}\left[s^E\sigma_0 + d\left(E, \sigma_0\right)E + \varepsilon_{irr}(E, \sigma_0)\right]. \tag{48}$$

It is illustrated in Section 6.1 that for data from York, spring constants on the order of 10 times physical values are required before (48) begins to differ significantly from (47). For regimes that require (47), the iterative fixed-point algorithm

$$\varepsilon^{n+1} = \frac{A}{A + s^E Lk}\left[s^E\sigma_0 + d\left(E, -L\varepsilon^n k/A + \sigma_0\right)E + \varepsilon\left(E, -L\varepsilon^n k/A + \sigma_0\right)\right]$$

can be used to efficiently compute strains as a function of E and σ_0.

To incorporate the damping element depicted in Figure 21(b), we include a damping force $F_d = -c\dot{u}$ in (45) to obtain the applied stress relation

$$\sigma = \frac{-L\varepsilon}{A}k - \frac{L\dot{\varepsilon}}{A}c + \sigma_0.$$

This then yields the differential equation

$$\frac{s^E Lc}{A + s^E Lk}\dot{\varepsilon} + \varepsilon = \frac{A}{A + s^E Lk}\left[s^E\sigma_0 + d\left(E, \sigma_0\right)E + \varepsilon_{irr}(E, \sigma_0)\right]. \tag{49}$$

which specifies strains produced by the actuator.

Figure 21: (a) PZT actuator with a prestress σ_0 and restoring spring, and (b) actuator that additionally incorporates a damping element.

5.2 Constitutive Relations for Distributed Models

The nature of inputs differs somewhat for distributed structures such as rods, beams, shells and membranes. To illustrate, consider a rod of length L as illustrated in Figure 22. The applied loads again are the field E and prestress σ_0 at the end of the rod. The development of PDE structural models requires the quantification of stresses along the rod length.

To determine whether strains or stresses should be considered as inputs for $0 < x < L$, we consider connections at $x = a$ that block rod movement. The stress σ_0 produces strains $\varepsilon(t, x)$ and displacements $u(t, x)$ for $x > a$ along with a stress $\sigma_0(t, a)$. Despite this stress, there are no strains nor displacements for $x \leq a$ due to the blocking elements. Hence strains rather than stresses should be considered as inputs along the rod so the independent variables for $0 < x < L$ are E and ε.

For this independent variable set, the appropriate thermodynamic potential is the electric Gibbs energy density

$$G_\alpha^e = \psi_\alpha - EP = G_\alpha + \sigma\varepsilon$$

(see pages 63-64 of [75]). To obtain appropriate constitutive relations, one can repeat the analysis of Section 4.1 using G_α^e rather than G_α. While fundamental in nature, this approach obscures a comparison with the constitutive relations (41) used to model (E, σ_0) inputs. Instead, we directly reformulate the relation (41) to provide stress as a function of strain.

To obtain an explicit constitutive equation, we assume that $|\sigma_0| >> |\sigma|$ for d and ε_{irr} defined in (42) and employ $d(E, \sigma_0)$ and $\varepsilon_{irr}(E, \sigma_0)$. Inversion of the strain relation in (41) then yields

$$\sigma(E, \varepsilon) = Y^E\varepsilon - e(E, \sigma_0)E - Y^E\varepsilon_{irr}(E, \sigma_0) \tag{50}$$

where

$$Y^E = \frac{1}{s^E} \quad , \quad e(E, \sigma_0) = \frac{1}{s^E}d(E, \sigma_0).$$

The constitutive relation (50) can be used to construct rod, beam and shell models for distributed structures. To illustrate, consider a rod having density ρ and cross-sectional area A. Longitudinal displacements are denoted by $u(t, x)$. As detailed in Chapter 7 of [75], force balancing yields

$$\rho A\frac{\partial^2 u}{\partial t^2} = \frac{\partial N}{\partial x}$$

where the force resultant is $N = \sigma A$. The stress is given by (50).

For general electro-elastic structures, one would employ the relations

$$\nabla \cdot D = 0 \quad , \quad D = \epsilon_0 E + P$$

$$\rho\ddot{u} = \nabla \cdot \sigma$$

$$\nabla \times E = 0 \quad , \quad E = -\nabla\varphi.$$

The use of (50) to construct models for PZT-based macro-fiber composite (MFC) actuators operating in highly hysteretic and nonlinear regimes is detailed in [32].

Figure 22: (a) Rod of length L with a connection at $x = a$ that blocks movement, and (b) displacement produced by a prestress σ_0.

6 Model Validation

The relations (40) or (41) characterize the polarizations and strains generated by fields or stresses applied to isolated ferroelectric materials. For actuators subjected to a prestress and restoring spring, the relations (47), (48) or (49) quantify the generated stresses whereas (50) provides a nonlinear constitutive relation for distributed structures. In this section, we illustrate the experimental validation of the model for a prestressed PZT element with a restoring spring, rate-dependent PZT, and PLZT subjected to various compressive prestresses.

Details regarding highly efficient implementation algorithms and data-driven parameter estimation techniques are provided in [31]. Additional examples illustrating the experimental validation of the model for PZT with variable loading rates and single crystal $BaTiO_3$ are provided in that paper.

6.1 Model Validation for a Prestressed PZT Actuator

We illustrate here validation of the model using data reported in [92] for a prestressed PZT actuator with a restoring spring. The multilayer actuator (NEC Model AEO505D08) employed the soft PZT material PIC151 and was comprised of 80 active layers, each having thickness 0.1 mm. The dimensions, including packaging, were $6.5 \times 6.5 \times 10$ mm which yielded the cross-sectional area $A = 42.25$ mm^2. Displacements were measured using a fiber-optic displacement sensor having an effective resolution of 0.1 μm and strains were computed by dividing the total thickness (8 mm) of the active layers. The data used for model validation was collected with a prestress of $\sigma_0 = -10.6$ MPa with a restoring spring having a stiffness $k = 2.7$ N/μm. The polarization was measured using a Sawyer-Tower circuit comprised of a reference capacitor connected in series with the PZT actuator. Strain and polarization data collected at a loading rate of $0.5\frac{\text{kV}}{\text{mm·s}}$ is plotted in Figure 23.

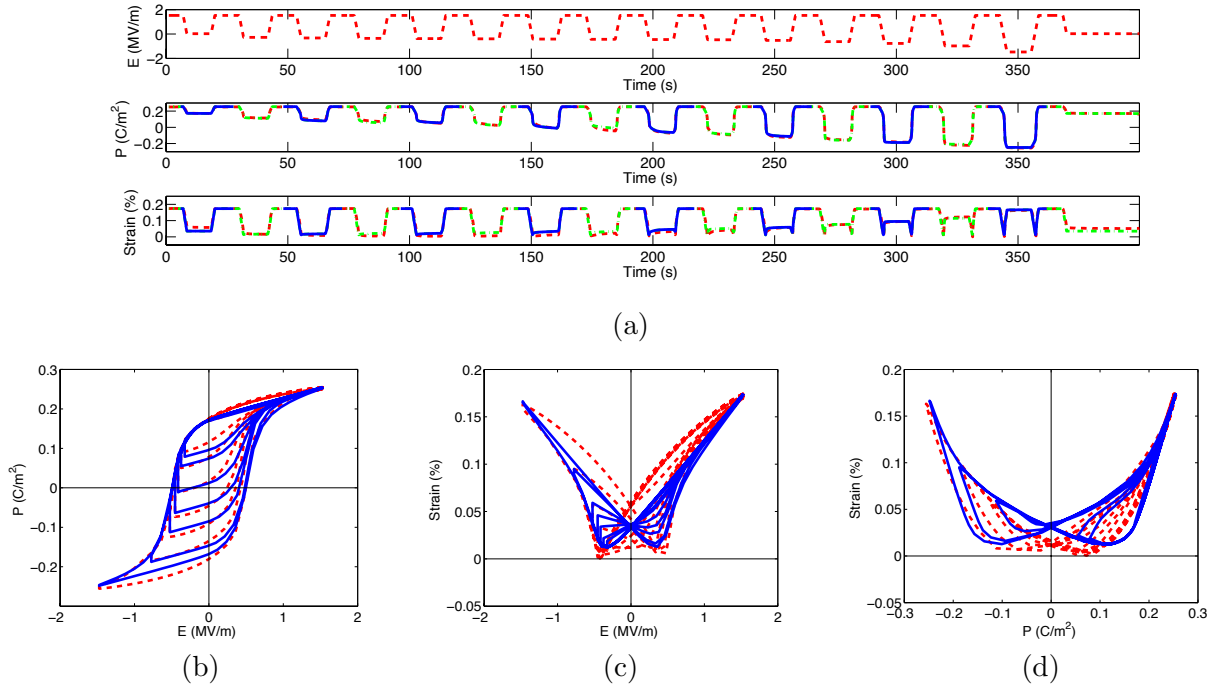

Figure 23: Fit of the polarization and strain model to data from [92] with a prestress of $\sigma_0 = -10.6$ MPa: (a) time domain and (b)-(d) phase space; (– – –) experimental data, (– • – •) model fit, (———) model fits for 8 selected loading cycles.

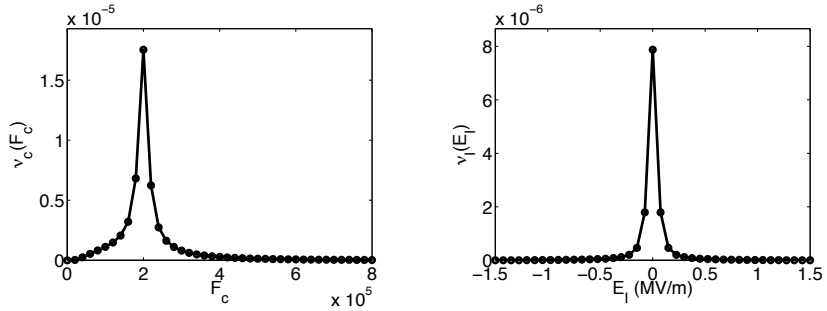

(a) (b)

Figure 24: (a) Critical driving force density $\nu_c(F_c)$ and (b) interaction field density $\nu_I(E_I)$ with 41 equally spaced quadrature points marked as dots.

In Figure 23(a), it is observed that following the application of a saturating 1.5 kV/mm field, fields were decreased and held at 15 different levels before being increased back to saturation. Depending on the held field value, this produced varying degrees of 90^o switching, that is manifested in the strain measurements, along with slower creep behavior in both the polarization and strain.

The polarization was modeled by the relation (41) and the strain by (48) with the measured field plotted in Figure 23(a) used as input. We neglected damping forces and the use of (49) due to the slow loading rate. For maximum strains on the order of $\varepsilon_{\max} = 0.0014$, $\left|\frac{-L\varepsilon_{\max}k}{A}\right| = 0.89$ MPa $<< |\sigma_0| = 10.6$ MPa, thus motivating the use of the linear relation (48) rather than the nonlinear relation (47). Further discussion detailing the validity of the linear strain relation for this actuator model is provided at the end of this section.

Use of the data-driven parameter estimation techniques discussed in [31] yielded the initial and optimized parameters summarized in Table 2 and the resulting model fits plotted in Figure 23. From Figure 23(a), it is observed that the model accurately characterizes both the switching and creep behavior of the polarization and strain as a function of time. To illustrate the E-P, E-ε and P-ε behavior, the loops indicated in Figure 23(a) were selected and plotted in Figures 23(b)-(d). The estimated interaction and coercive field densities ν_I and ν_c are plotted in Figure 24. The reader is referred to [31] for statistical properties of the densities.

	P_R^+	ε_R^+	ε_R^{90}	χ_+^σ	d_+	s_+^E	γ	τ_{90}	τ_{180}
Init	0.18	0.056×10^{-2}	0.0×10^{-2}	5.13×10^{-8}	374×10^{-12}	1.88×10^{-11}	5.70×10^{-5}	1.40	0.140
Opt	0.18	0.054×10^{-2}	-0.052×10^{-2}	5.04×10^{-8}	917.74×10^{-12}	2.25×10^{-11}	1.82×10^{-3}	1.39	0.024

Table 2: Initial and optimized parameter values for the 90° model with $\sigma_0 = -10.6$ MPa. The optimized density parameter values $\alpha_1 = 2.58, \alpha_0 = 1.66, \alpha_{-1} = 2.01, \alpha_{-2} = 2.10, \alpha_{-3} = 2.03$ and $\beta_1 = 1.12, \beta_0 = 0.71, \beta_{-1} = 2.01, \beta_{-2} = 4.39, \beta_{-3} = 5.79$ were obtained using initial estimates of 1.

Linear Versus Nonlinear Strain Relations

It was noted that for $k = 2.7$ N/μm and $\sigma_0 = -10.6$ MPa, $\left|\frac{L\varepsilon k}{A}\right| << |\sigma_0|$ which permits the nonlinear strain relation (47) to be approximated by the explicit relation (48). Here we quantify the accuracy of (48) as a function of the spring constant and prestress level for the considered actuator configuration.

We first define the relative errors

$$e_P = \frac{||P^L - P^N||_2}{||P^N||_2} \times 100 \quad , \quad e_\varepsilon = \frac{||\varepsilon^L - \varepsilon^N||_2}{||\varepsilon^N||_2} \times 100$$

where P^N, ε^N and P^L, ε^L respectively denote the polarization and strain values given by (48) and (47) and $\|\cdot\|_2$ is the L_2 norm. The relative errors obtained by using the estimated polarization values summarized in Table 2 are compiled in Table 3 for various combinations of k and σ_0. It is observed that for prestresses less than -32 MPa and spring constants less than 27 N/μm, the linear relation provides suitable accuracy.

Prestress	$k = 0.27$ $N/\mu m$	$k = 2.7$ $N/\mu m$	$k = 5.4$ $N/\mu m$	$k = 27$ $N/\mu m$
-2 MPa	(0.0049, 0.0059)	(0.0489, 0.0584)	(0.0969, 0.1157)	(0.4462, 0.5438)
-4 MPa	(0.0047, 0.0059)	(0.0464, 0.0589)	(0.0919, 0.1171)	(0.4223, 0.5489)
-8 MPa	(0.0042, 0.0061)	(0.0415, 0.0603)	(0.0820, 0.1193)	(0.3774, 0.5602)
-16 MPa	(0.0034, 0.0063)	(0.0331, 0.0625)	(0.0654, 0.1238)	(0.3013, 0.5856)
-32 MPa	(0.0032, 0.0072)	(0.0321, 0.0719)	(0.0638, 0.1434)	(0.2960, 0.6794)

Table 3: Relative error (e_P, e_ε) between the linear relation (48) and nonlinear relation (47).

6.2 Model Validation for Rate-Dependent Bulk PZT

Soft ferroelectric compounds have lower coercive fields, more hysteresis loss, and larger susceptibilities and piezoelectric constants than hard compounds. Here we illustrate the performance of the model for characterizing the rate-dependence of the soft PZT material PIC151 which has the composition $Pb(Ni_{1/3}\ Sb_{2/3})O_3$-$PbTiO_3$-$PbZrO_3$ ternary phase system that includes about 2-3% $Pb(Ni_{1/3}\ Sb_{2/3})O_3$ near the morphotropic phase boundary of PZT. We compare to data reported in [96], that was collected at rates of 0.01 Hz, 0.1 Hz and 1 Hz, as shown in Figure 3. The PZT in this case was a $5 \times 5 \times 15$ mm^3 cube that was cut from a bulk ferroelectric speciman and electroded at the ends. Hence the construction and electrode configuration differ from the multilayer actuator discussed in Section 6.1.

It is observed that coercive fields increase as the frequency increases and that both the polarization and strain continue to increase when the field is reversed at its maximal values of 2 kV/mm. This is due to the fact that dipoles do not switch instantaneously as modeled by the relations $\frac{1}{\tau_{90}}$ and $\frac{1}{\tau_{180}}$ in the likelihood relations (34). Hence some dipoles will continue to switch from -180^o to 90^o and 90^o to 180^o during the initial unloading process. This rate-dependence is due to the time scale difference between dipole kinetics and electrical or mechanical loading rates.

The initial and optimized parameters estimated through a fit to 0.1 Hz and 1.0 Hz loading rates are reported in Table 4 and the corresponding model fits are shown in Figure 25 along with the model predictions at 0.1 Hz. It is observed that the coercive field increase and rate-dependence of the polarization is accurately modeled at all three frequencies. The modeled polarization and strain behavior are also quite accurate including the nearly parabolic and anhysteretic 1 Hz P-ε behavior

	P_R^+	ε_R^+	ε_R^{90}	χ_+^σ	d_+	γ	τ_{90}	τ_{180}
Init	0.3	0.25×10^{-2}	-0.5×10^{-2}	2.35×10^{-8}	374×10^{-12}	0.2×10^{-4}	0.67	0.067
Opt	0.28	0.22×10^{-2}	-0.84×10^{-2}	0.70×10^{-8}	378.47×10^{-12}	1.83×10^{-4}	0.031	0.13

Table 4: Initial and optimized PZT parameter values estimated through a fit to the 0.1 Hz and 1.0 Hz data from [96]. Density parameters: $\bar{F}_c = 0.66 \times 10^6, \sigma_I = 0.5 \times 10^6, \sigma_c = 0.35$ and $\alpha_1 = 1.02, \alpha_0 = 1.04, \alpha_{-1} = 0.98, \alpha_{-2} = 1.13, \alpha_{-3} = 1.23, \beta_1 = 0.77, \beta_0 = 0.86, \beta_{-1} = 1.34, \beta_{-2} = 1.80, \beta_{-3} = 1.90, \beta_{-4} = 2.36$.

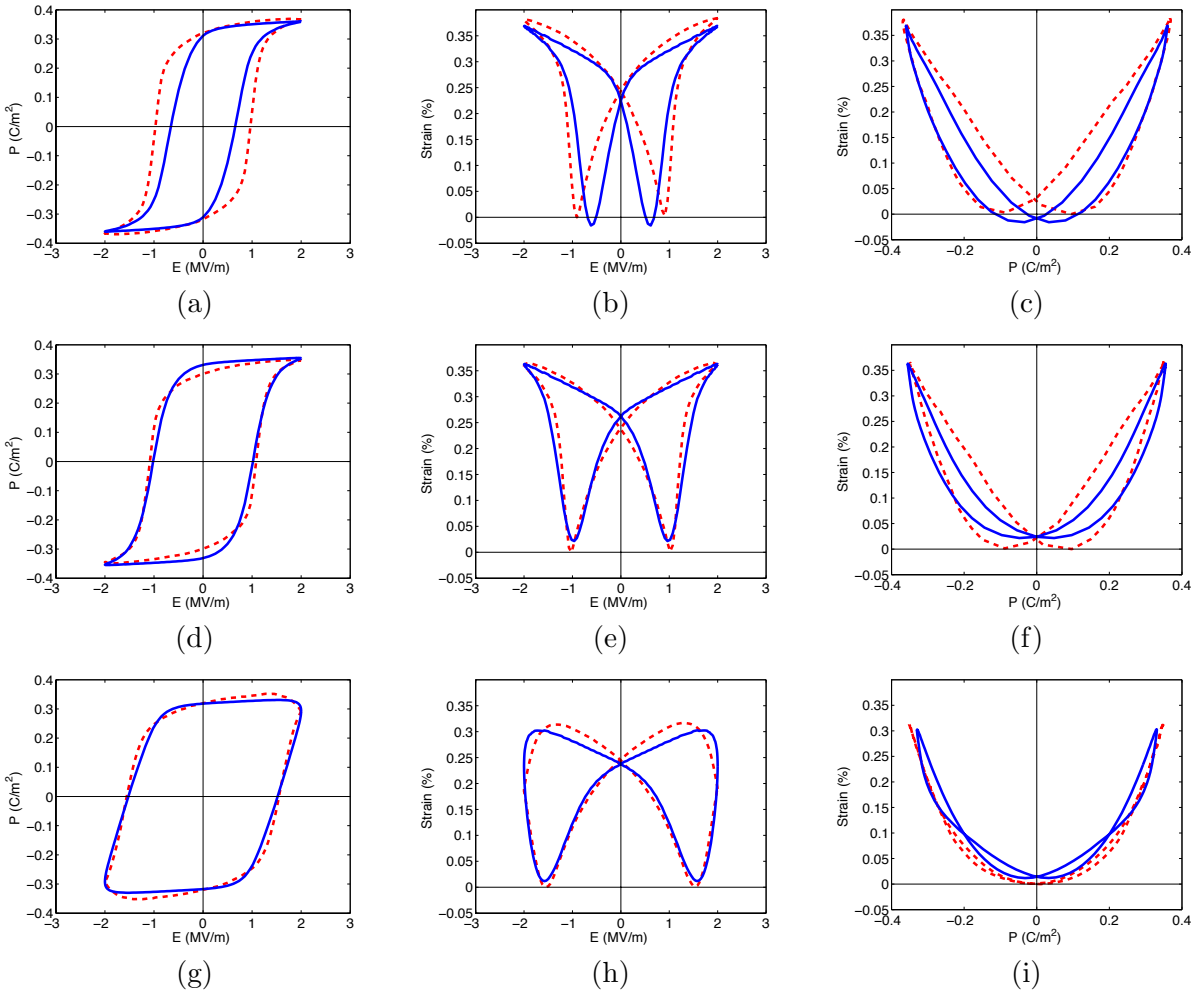

Figure 25: Fit of the polarization and strain model to data from [96] for loading rates of (d)-(f) 0.1 Hz and (g)-(i) 1 Hz. Model prediction for (a)-(c) 0.01 Hz: (– – –) experimental data, (———) model fit.

which we note was modeled using linear domain-level constitutive relations in combination with grain-level switching mechanisms. It is observed that whereas the model fit is quite accurate at 1 Hz, the model does not incorporate the degree of delayed dipole switching as is exhibited by the data. This indicates that aspects of the 90^o switching model can still be improved.

A comparison between the quasistatic hysteresis and butterfly loops for the prestressed multilayer actuator and bulk sample, respectively plotted in Figures 23 and 25, reveal differences in the remanence values, coercive fields, and post-switching slopes. This is substantiated by differences in the optimized parameter values in Tables 2 and 4. This is due in part to differences in the actuator construction and drive configuration and it illustrates the necessity of calibrating models for a specific actuator configuration.

6.3 Model Validation for PLZT

As noted in Section 2.2, 8/65/35 PLZT has a rhombohedral crystal structure so switches of 70.5^o and 109.5^o produce strains and changes in the polarization. This can be modeled two ways using the homogenized energy model. The more rigorous is to modify the energy landscape so that it

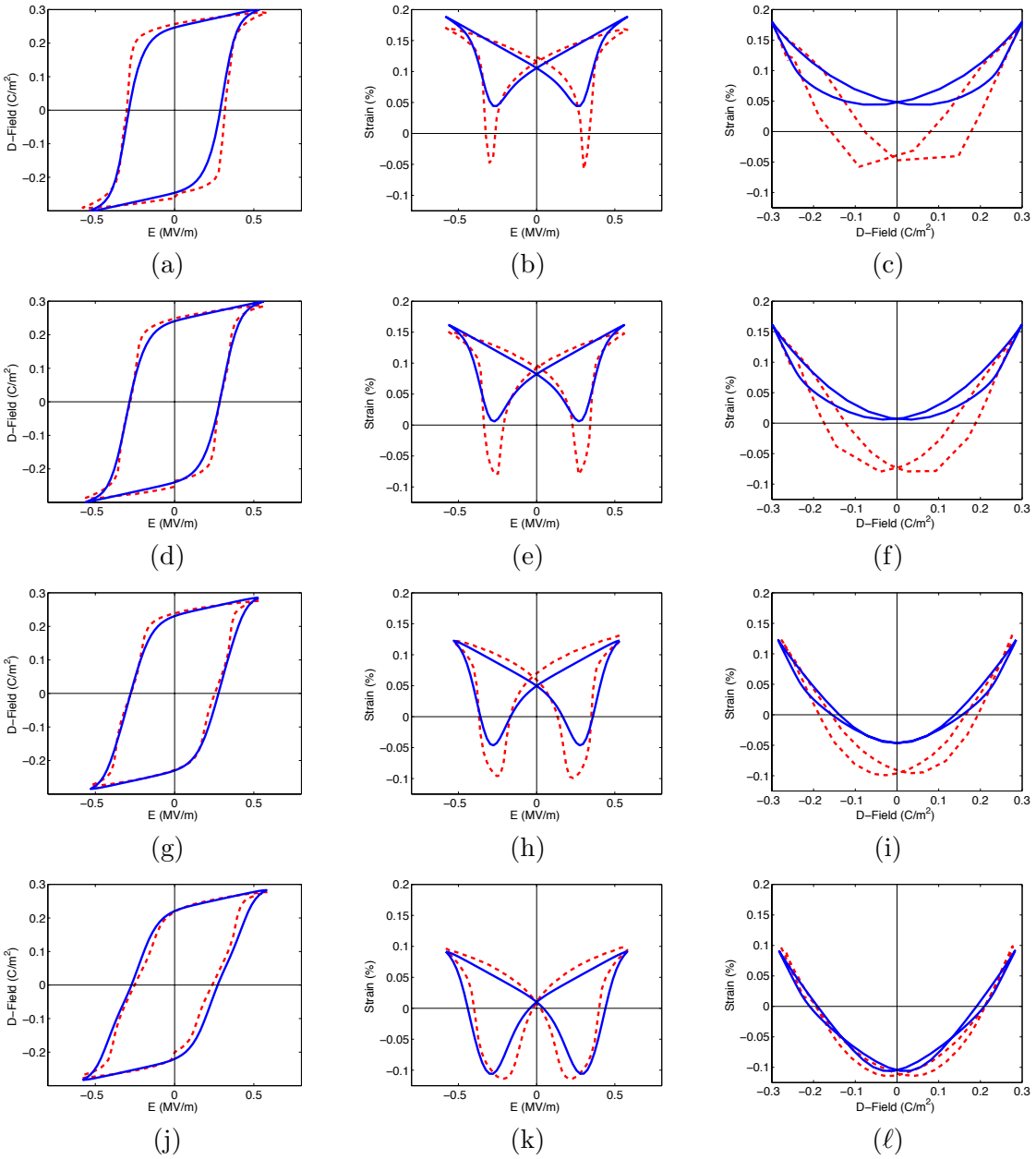

Figure 26: Fit of the D-field and strain model to data from Lynch [61]: (a)-(c) $\sigma_0 = -3$ MPa and (j)-(ℓ) $\sigma_0 = -15$ MPa. Model predictions for prestresses of (d)-(f) $\sigma_0 = -6$ MPa and (g)-(i) $\sigma_0 = -10$ MPa; (– – –) experimental data, (———) model fit and predictions.

has minima at $\alpha = \pm 180, 70.5$ and 109.5. Alternatively, one can apply the tetragonal model with $\alpha = \pm 180$ and 90 in a phenomenological manner to model the stress-dependence of the strains and polarization. We illustrate the accuracy of the latter approach through fits and predictions using PLZT data collected at various prestresses as reported in [61].

To estimate model parameters, we first fit the polarization and strain model (41) to data collected at prestresses of $\sigma_0 = -3$ MPa and $\sigma_0 = -15$ MPa; note that Lynch reports D-field data rather than polarization so modeled results were obtained using the relation $D = \varepsilon_0 E + P$. This yielded the parameters summarized in Table 5 and the model fits shown in Figure 26(a)-(c) and (j)-(ℓ). The

model with these parameters was then used to predict the responses for prestresses of $\sigma_0 = -6$ MPa and $\sigma_0 = -10$ MPa yielding the results shown in Figure 26(d)-(i). The model underpredicts the amount of non-180^o switching in the strain model with $\sigma_0 = -3$ MPa, which may be due in part to the use of tetragonal rather than rhombohedral energy landscapes, but accurately fits and predicts the switching behavior at other stress levels.

It is observed that the model reasonably characterizes the nearly quadratic D-ε behavior despite the fact that it employs linear constitutive relations rather than quadratic electrostrictive relations. As detailed in Section 2.2, the quadratic strain behavior for this material is due to dipole rotation rather than classical electrostrictive effects so the homogenized energy model, which employs energy landscapes to quantify dipole switching, provides reasonably accurate material characterization.

	P_R^+	ε_R^+	ε_R^{90}	χ_+^σ	d_+	s_+^E	γ	τ_{90}	τ_{180}
Init	0.25	0.09×10^{-2}	-0.1×10^{-2}	7.03×10^{-8}	682×10^{-12}	14.7×10^{-12}	2.0×10^{-3}	0.03	0.003
Opt	0.24	0.13×10^{-2}	-0.03×10^{-2}	10.06×10^{-8}	1390.5×10^{-12}	71.93×10^{-12}	9.62×10^{-4}	0.032	0.70

Table 5: Initial and optimized PLZT parameter values for the 90^o model fitting two intermediate prestress levels $\sigma_0 = -3$MPa and $\sigma_0 = -15$ MPa.

7 Concluding Remarks

Hysteresis, which is intrinsic to ferroelectric materials, involves multiple spatial and temporal scales. At the domain level, strains or changes in polarization are due to stress-induced material deformations or field-induced ion movement and the behavior is often reversible and linear. Field or stress-induced dipole switching at the grain level produces irreversible hysteresis in both the field-polarization and field-strain relations. For single crystal materials comprised of a single grain, the switching is typically rapid thus producing sharp hysteresis and butterfly loops in quasistatic operating regimes. For polycrystalline materials with distributed interaction and coercive fields, hysteresis and butterfly loops are smoothed due to nonuniform grain contributions. The behavior of hysteresis loops is further modified when hysteretic actuator or sensor materials are employed on distributed structures. Hence the nature of the hysteretic response is highly influenced by the spatial scale under consideration.

Furthermore, ferroelectric materials exhibit creep and rate-dependent effects even at low frequencies. This is due to the fact that the kinetics associated with dipole switching typically differs from mechanical or electrical loading rates. This establishes multiple time scales that must be incorporated in dynamic models.

The homogenized energy model is a multiscale, microscopically-motivated or micromechanical approach that incorporates the rate-dependence and multiple timescales exhibited by materials. At the domain level, the minimization of Gibbs energy densities yields linear constitutive relations. At the grain level, dipole fractions serve as appropriate, physically-motivated, internal variables to quantify the timescales and hysteresis associated with dipole switching. The dynamics of dipole fractions are governed by evolution equations driven by likelihood rates constructed using Boltzmann theory to quantify the scaled probability of transitioning between stable equilibria associated with dipole variants. Macroscale models are developed by assuming that properties such as coercive fields, critical driving forces, and interaction fields are manifestations of underlying densities rather than constants. Finally, it is shown that the homogenized energy model framework facilitates subsequent development of distributed system models. The complete multiscale development is illustrated in Figure 4.

In Section 2, significant discussion was devoted to mechanisms that produce the quadratic P-ε or D-ε behavior exhibited by ferroelectric materials. For compounds such as PMN, this is due to classical electrostriction and quadratic domain-level constitutive relations are required to model the nearly anhysteretic field-strain behavior. In other materials, such as PZT, this is due to domain rotation and the model validation results illustrate that highly accurate material characterization can be achieved using linear domain level relations.

The validation results of Section 6 demonstrate the capability of the model to characterize major and biased minor polarization and strain loops, the effect of prestresses, and creep and rate-dependencies for PZT and PLZT. Additional validation results demonstrating the performance of the framework for characterizing single crystal $BaTiO_3$ and variable loading rates in PZT are presented in the companion paper [31]. It is also shown in [31] that due to its energy basis, the model admits highly efficient implementation and data-driven algorithms to determine initial parameter estimates based on measured properties of the data. This facilitates model calibration and implementation for design and control of devices and complex structures arising in applications.

We note that the polarization model (26) bears some resemblance to a Preisach model. In the absence of thermal activation, (26) satisfies congruency and deletion properties and hence it provides an energy-based derivation for certain classical Preisach models. As detailed in [75], extended Preisach formulations have been developed to incorporate rate effects, thermal activation and creep. However, they do so by modifying the densities rather than using energy and kinetics principles to incorporate them in the kernels as is the case for the homogenized energy model. Moreover, the combined strain and polarization relations that result from the inclusion of elastic, electric, and coupling components in the domain-level Gibbs energy density yield macroscale constitutive relations that incorporate significantly more physics than Preisach-based approaches.

An issue that is of significant interest for control design of systems with hysteretic actuators and sensors concerns the construction of approximate inverse models. For the homogenized energy framework, initial approximate inverse models have been implemented at rates that are proven no slower than 1/6-1/7 the rate of forward simulations. The completion of these algorithms and their incorporation in robust control designs constitutes present and future research.

A Available Codes

To facilitate model validation and dissemination to the community, we have made codes and data available at the website `http://www4.ncsu.edu/~jhcrews/smart/code/pzt/index.html`.

Acknowledgements

This research was supported in part by the Air Force Office of Scientific Research through the grants AFOSR FA9550-08-1-0348, AFOSR FA9550-11-10152 and the NSF grant NSF DMS-0636590 EMSW21-RTG. The authors gratefully thank Alex York for providing the PZT data used for validation in Section 6.1. We also thank John Crews for providing detailed feedback regarding the paper.

References

[1] M. Achenbach and I. Müller, "Simulation of material behavior of alloys with shape memory," *Archives of Mechanics*, 37(6), pp. 573–585, 1985.

[2] M. Al Janaideh, S. Rakheja and C-Y. Su, "A generalized Prandtl-Ishlinskii model for characterizing the hysteresis and saturation nonlinearities of smart actuators," *Smart Materials and Structures*, 18, 045001, 2009.

[3] M. Al Janaideh, C-Y. Su and S. Rakheja, "Development of the rate-dependent Prandtl-Ishlinskii model for smart actuators," *Smart Materials and Structures*, 17, 035026, 2008.

[4] J.C. Anderson, *Dielectrics*, Reinhold Publishing Corporation, New York, 1964.

[5] A. Arockiarajan, B. Delibas, A. Menzel and W. Seemann, "Studies on rate-dependent switching effects of piezoelectric materials using a finite element model," *Computational Materials Science*, 37, pp. 307–317, 2006.

[6] C.A. Balanis, *Advanced Engineering Electromagnetics*, John Wiley and Sons, New York, 1989.

[7] B.L. Ball, R.C. Smith, S-J. Kim and S. Seelecke, "A stress-dependent hysteresis model for ferroelectric materials," *Journal of Intelligent Material Systems and Structures*, 18(1), pp. 69–88, 2007.

[8] D. Belincourt and H. Jaffe, "Elastic and piezoelectric coefficients of single-crystal barium titanate," *Physical Review*, 111(1), pp. 143–148, 1958.

[9] A.Y. Belov and W.S. Kreher, "Viscoplastic behavior of perovskite type ferroelectrics," *Materials Science and Engineering B*, 118, pp. 7–11, 2005.

[10] G. Bertotti, *Hysteresis in Magnetism*, Academic Press, San Diego, CA, 1998.

[11] K. Bhattacharya and G. Ravichandran, "Ferroelectric perovskites for electromechanical actuation," *Acta Materialia*, 51, pp. 5941–5960, 2003.

[12] O. Bilgen, C. De Marqui, Jr., K.B. Kochersberger and D.J. Inman, "Macro-fiber composite actuators for flow control of a variable camber airfoil," *Journal of Intelligent Material Systems and Structures*, 22(1), pp. 81–91, 2011.

[13] T.R. Braun and R.C. Smith, "High speed model implementation and inversion techniques for ferroelectric and ferromagnetic transducers," *Journal of Intelligent Material Systems and Structures*, 19(11), pp. 1295–1310, 2008.

[14] M. Brokate and J. Sprekels, *Hysteresis and Phase Transitions*, Springer-Verlag, New York, 1991.

[15] E. Burcsu, G. Ravichandran and K. Bhattacharya, "Large electrostrictive actuation of barium titanate single crystals," *Journal of the Mechanics and Physics of Solids*, 52, pp. 823–846, 2004.

[16] W.G. Cady, *Piezoelectricity*, McGraw-Hill Book Company, Inc., New York, 1946.

[17] M.E. Caspari and W.J. Merz, "The electromechanical behavior of $BaTiO_3$ single-domain crystals," *Physical Review*, 80(6), pp. 1082–1089, 1950.

[18] S. Chikazumi, *Physics of Ferromagnetism*, Second Edition, English edition prepared with the assistance of C.D. Graham, Jr., Clarendon Press, Oxford, 1997.

[19] A.C.F. Cocks and R.M. McMeeking, "A phenomenological constitutive law for the behavior of ferroelectric ceramics," *Ferroelectrics*, 228, pp. 219–228, 1999.

[20] J.H. Crews, R.C. Smith, K.M. Pender, J.C. Hannen and G.D. Buckner, "Data-driven techniques to estimate parameters in the homogenized energy model for shape memory alloys," CRSC Technical Report CRSC-TR11-15, *Journal of Intelligent Material Systems and Structures*, submitted.

[21] E. Della Torre, *Magnetic Hysteresis*, IEEE Press, New York, 1999.

[22] A.F. Devonshire, "Theory of ferroelectrics," *Philosophical Magazine*, 3(10), pp. 85–130, 1954.

[23] R.S. Elliott, *Electromagnetics: History, Theory and Applications*, IEEE Press, Piscataway, NJ, 1993.

[24] J.M. Ernstberger, *High Speed Parameter Estimation for a Homogenized Energy Model,* PhD Dissertation, North Carolina State University, Raleigh, NC, 2008.

[25] N. Goldenfeld, *Lectures on Phase Transitions and the Renormalization Group,* Addison-Wesley, Reading, MA, 1992.

[26] J. Grindlay, *An Introduction to the Phenomenological Theory of Ferroelectricity,* Pergamon Press, Oxford, 1970.

[27] T. Hegewald, B. Kaltenbacher, M. Kaltenbacher and R. Lerch, "Efficient modeling of ferroelectric behavior for the analysis of piezoceramic actuators," *Journal of Intelligent Material Systems and Structures*, 19, pp. 1117–1129, 2008.

[28] K. Hoffman and R.J. Wood, "Myriapod-like ambulation of a segmented microrobot," *Autonomous Robots*, 31(1), pp. 103–114, 2011.

[29] C.L. Hom and N. Shankar, "Modeling nonlinearity in electrostrictive sonar transducers," *Journal of the Acoustical Society of America*, 104(4), pp. 1903–1913, 1998.

[30] Z. Hu, R.C. Smith and J.M. Ernstberger, "Data driven techniques to estimate parameters in a rate-dependent ferromagnetic hysteresis model," *Physica B*, to appear.

[31] Z. Hu, R.C. Smith, J.M. Ernstberger, "The homogenized energy model (HEM) for characterizing polarization and strains in hysteretic ferroelectric materials: Implementation algorithms and data-driven parameter estimation techniques," *Journal of Intelligent Material Systems and Structures*, submitted.

[32] Z. Hu, R.C. Smith, M. Hays and W.S. Oates, "Statistical parameter estimation and uncertainty quantification for macro fiber composite actuators operating in nonlinear and hysteretic regimes," Proceedings of the 50th IEEE Conference on Decision and Control and European Control Conference, Orlando, FL, December 12-15, pp. 2764–2769. 2011.

[33] J.E. Huber, "Micromechanical modelling of ferroelectrics," *Current Opinion in Solid State and Materials Science*, 9, pp. 100-106, 2005.

[34] J.E. Huber and N.A. Fleck, "Ferroelectric switching: a micromechanics model versus measured behavior," *European Journal of Mechanics A/Solids*, 23, pp. 203–217, 2004.

[35] J.E. Huber, N.A. Fleck, C.M. Landis and R.M. McMeeking, "A constitutive model for ferroelectric polycrystals," *Journal of the Mechanics and Physics of Solids*, 47, pp. 1663–1697, 1999.

[36] S.C. Hwang, C.S. Lynch and R.M. McMeeking, "Ferroelectric/ferroelastic interactions and a polarization switching model," *Acta Matellurgica et Materialia*, 43, pp. 2048–2073, 1995.

[37] K. Jayabal, A. Menzel, A. Arockiarajan and S.M. Sivakumar, "Micromechanical modelling of switching phenomena in polycrystalline piezoceramics. Application of a polygonal finite element approach," *Computational Mechanics*, 48, pp. 421–435, 2011.

[38] K. Jayabal, D. Srikrishna, T.S. Abhinandan, A. Arockiarajan and S.M. Sivakumar, "A thermodynamically consistent model with evolving domain structures in ferroelectrics," *International Journal of Engineering*, 47(10), pp. 1014–1024, 2009.

[39] D.C. Jiles, *Introduction to Magnetism and Magnetic Materials*, Chapman and Hall, New York, 1991.

[40] F. Jona and G. Shirane, *Ferroelectric Crystals*, Dover Publications, Inc., New York, 1993.

[41] M. Kaltenbacher, B. Kaltenbacher, T. Hegewald and R. Lerch, "Finite element formulation for ferroelectric hysteresis of piezoelectric materials," *Journal of Intelligent Material Systems and Structures*, 21, pp. 773–785, 2010.

[42] M. Kamlah, "Ferroelectric and ferroelastic piezoceramics — modeling and electromechanical hysteresis phenomena," *Continuum Mechanics and Thermodynamics*, 13, pp. 219–268, 2001.

[43] M. Kamlah and U. Böhle, "Finite element analysis of piezoceramic components taking into account ferroelectric hysteresis behavior,"" *International Journal of Solids and Structures*, 38, pp. 605-633, 2001.

[44] M. Kamlah and Q. Jiang, "A constitutive model for ferroelectric PZT ceramics under uniaxial loading," *Smart Materials and Structures*, 8, pp. 441–459, 1999.

[45] M. Kamlah and C. Tsakmakis, "Phenomenological modeling of the nonlinear electro-mechanical coupling in ferroelectrics," *International Journal of Solids and Structures*, 36, pp. 669–695, 1999.

[46] S.-J. Kim, "A prediction of rate-dependent behavior in ferroelectric polycrystals," *Materials Science and Engineering B*, 141, pp. 34–42, 2007.

[47] S.-J. Kim and S. Seelecke, "A rate-dependent three-dimensional free energy model for ferroelectric single crystals," *International Journal of Solids and Structures*, 44, pp. 1196–1209, 2007.

[48] K. Kuhnen and P. Krejci, "Compensation of complex hysteresis and creep effects in piezoelectrically actuated systems — A new Preisach modeling approach," *IEEE Transactions on Automatic Control*, 54(3), pp. 537–550, 2009.

[49] V. Kumar, M. Hays, E. Fernandez, W. Oates and F.S. Alvi, "Flow sensitive actuators for micro-air vehicles," *Smart Materials and Structures*, 20, 105033, 2011.

[50] C.M. Landis, "A new finite-element formulation for electromechanical boundary value problems," *International Journal for Numerical Methods in Engineering*, 55, pp. 613–628, 2002.

[51] C.M. Landis, "Non-linear constitutive modeling of ferroelectrics," *Current Opinion in Solid State and Materials Science,* 8, pp. 59–69, 2004.

[52] C.M. Landis and R.M. McMeeking, "A phenomenological constitutive law for ferroelastic switching and a resulting asymptotic crack tip solution," *Journal of Intelligent Material Systems and Structures*, 10, pp. 155–163, 2000.

[53] D.J. Leo, *Engineering Analysis of Smart Material Systems*, John Wiley and Sons, Inc., Hoboken, NJ, 2007.

[54] S. Li, A.S. Bhalla, R.E. Newnham and L.E. Cross, "90^o domain reversal in $Pb(Zr_xTi_{1-x}O_3$ ceramics," *Journal of Materials Science*, 29, pp. 1290–1294, 1994.

[55] Z. Li, S.-K. Chan, M.H. Grimsditch and E.S. Zouboulis, "The elastic and electromechanical properties of tetragonal $BaTiO_3$ single crystals," *Journal of Applied Physics*, 70(12), pp. 7327–7332, 1991.

[56] F. Li and D. Fang, "Simulations of domain switching in ferroelectrics by a three-dimensional finite element model," *Mechanics of Materials*, 36, pp. 959–973, 2004.

[57] J.P. Lien, A. York, T. Fang and G.D. Buckner, "Modeling piezoelectric actuators with hysteretic recurrent neural networks," *Sensors and Actuators A: Physical*, 163, pp. 516–525, 2010.

[58] M.E. Lines and A.M Glass, *Principles and Applications of Ferroelectrics and Related Materials*, Oxford University Press, Oxford, UK, 1977, Oxford Classics Series, 2001.

[59] K. Linnemann, S. Klinkel and W. Wagner, "A constitutive model for magnetostrictive and piezoelectric materials," *International Journal of Solids and Structures*, 46, pp. 1149–1166, 2009.

[60] W. Lu, D.N. Fang, C.Q. Li, K.C. Hwang, "Nonlinear electric-mechanical behavior and micromechanics modelling of ferroelectric domain evolution," *Acta Materialia*, 47, pp. 2913–2926, 1999.

[61] C.S. Lynch, "The effect of uniaxial stress on the electro-mechanical response of 8/65/35 PLZT, *Acta Materialia*, 44(10), pp. 4137–4148, 1996.

[62] J.A. Main, D. Newton, L. Massengil and E. Garcia, "Efficient power amplifiers for piezoelectric applications," *Smart Materials and Structures*, 5(6), pp. 766–775, 1996.

[63] W.P. Mason, "Electrostrictive effect in barium titanate ceramics," *Physical Review*, 74(9), pp. 1134–1147, 1948.

[64] W.P. Mason, *Physical Acoustics and the Properties of Solids,* D. Van Nostrand Company, Inc., New York, 1958.

[65] C. Miehe and D. Rosato, "A rate-dependent incremental variational formulation of ferroelectricity," *International Journal of Engineering Science*, 49, pp. 466–496, 2011.

[66] A.J. Moulson and J.M. Herbert, *Electroceramics: Materials, Properties, Applications*, Chapman and Hall, New York, 1990.

[67] J. Nuffer and T. Bein, "Applications of piezoelectric materials in the transportation industry," Global Symposium on Innovative Solutions for the Advancement of the Transport Industry, San Sebastian, Spain, 2006.

[68] N.O. Pérez-Arancibia, K.Y. Ma, K.C. Galloway, J.D. Greenberg and R.J. Wood, "First controlled vertical flight of a biologically inspired microrobot," *Bioinspiration and Biomimetics*, 6, 036009, 2011.

[69] M.B. Rauls, W. Dong, J.E. Huber and C.S. Lynch, "The effect of temperature on the large field electromechanical response of relaxor ferroelectric 8/65/35 PLZT," *Acta Materialia*, 2011, to appear.

[70] J.F. Scott, *Ferroelectric Memories*, Springer, Berlin, 2000.

[71] S. Seelecke, S-J. Kim, B. Ball and R.C. Smith, "A rate-dependent two-dimensional free energy model for ferroelectric single crystals," *Continuum Mechanics and Thermodynamics*, 17(4), pp.337–350, 2005.

[72] S. Seelecke and I. Müller, "Shape memory alloy actuators in smart structures — Modeling and simulation," *ASME Applied Mechanics Reviews*, 57(1), pp. 23–46, 2004.

[73] J. Shieh, J.E. Huber and N.A. Fleck, "An evaluation of switching criteria for ferroelectrics under stress and electric field," *Acta Materialia*, 51, pp. 6123–6137, 2003.

[74] D. Shilo, E. Burcsu, G. Ravichandran and K. Bhattacharya, "A model for large electrostrictive actuation in ferroelectric single crystals," *International Journal of Solids and Structures*, 44, pp. 2053–2065, 2007.

[75] R.C. Smith, *Smart Material Systems: Model Development*, SIAM, Philadelphia, PA, 2005.

[76] R.C. Smith, M.J. Dapino and S. Seelecke, "A free energy model for hysteresis in magnetostrictive transducers," *Journal of Applied Physics*, 93(1), pp. 458–466, 2003.

[77] R.C. Smith, M.J. Dapino, T.R. Braun and A.P. Mortensen, "A homogenized energy framework for ferromagnetic hysteresis," *IEEE Transactions on Magnetics*, 42(7), pp. 1747–1769, 2006.

[78] R.C. Smith, A.G. Hatch, B. Mukherjee and S. Liu, "A homogenized energy model for hysteresis in ferroelectric materials: General density formulation," *Journal of Intelligent Material Systems and Structures*, 16(9), pp. 713-732, 2005.

[79] R.C. Smith, S. Seelecke, M.J. Dapino and Z. Ounaies, "A unified framework for modeling hysteresis in ferroic materials," *Journal of the Mechanics and Physics of Solids*, 54(1), pp. 46-85, 2005.

[80] R.C. Smith, S. Seelecke, Z. Ounaies and J. Smith, "A free energy model for hysteresis in ferroelectric materials," *Journal of Intelligent Material Systems and Structures*, 14(11), pp. 719–739, 2003.

[81] Y.C. Shu and K. Bhattacharya, "Domain patterns and macroscopic behaviour of ferroelectric materials," *Philosophical Magazine B*, 81(12), pp. 2021–2054, 2001.

[82] H.J. Song, Y-T. Choi, N.M. Wereley and A.S. Purekar, "Energy harvesting devices using macro-fiber composite materials," *Journal of Intelligent Material Systems and Structures*, 21(6), pp. 647–658.

[83] Y. Su and G.J. Weng, "A polycrystal hysteresis model for ferroelectric ceramics," *Proceedings of the Royal Society A*, 462, pp. 1573–1592, 2006.

[84] T. Tsurumi, Y. Kumano, N. Ohashi, T. Takenaka and O. Fukunaga, "90^o domain reorientation and electric-field-induced strain of tetragonal lead zirconate titanate ceramics," *Japanese Journal of Applied Physics*, 36, Part 1, No. 9B, pp. 5970–5975, 1997.

[85] K. Uchino, *Ferroelectric Devices*, 2nd Edition, CRC Press/Taylor and Francis, Boca Raton, FL, 2010.

[86] K. Uchino and J.R. Giniewicz, *Micromechatronics*, Marcel Dekker, Inc., New York, 2003.

[87] D. Vasic, E. Sarraute, F. Costa, P. Sangouard and E. Cattan, "Piezoelectric micro-transformer based on PZT unimorph membrane," *Journal of Micromechanics and Microengineering*, 14, S90–S96, 2004.

[88] W. Voigt, *Lehrbuch der Kristallphysik*, B.G. Teubner, Leipzig, Berlin, 1928.

[89] J. Wang, S-Q. Shi, L-Q. Chen, Y. Li and T-Y. Zhang, "Phase field simulations of ferroelectric/ferroelastic polarization switching," *Acta Materialia*, 52, pp. 749–764, 2004.

[90] R.J. Wood, "The first takeoff of a biologically inspired at-scale robotic insect," *IEEE Transactions on Robotics*, 24(2), pp. 341–347, 2008.

[91] R.J. Wood, B. Finio, M. Karpelson, K. Ma, N.O. Pérez-Arancibia, P.S. Sreetharan, H. Tanaka and J.P. Whitney, "Progress on 'pico' air vehicles," International Symposium on Robotics Research, Flagstaff, AZ, August 2011.

[92] A. York, *Experimental characterization and modeling of electro-mechanically coupled ferroelectric actuators,* PhD Dissertation, North Carolina State University, Raleigh, NC, 2008.

[93] A. York and S. Seelecke, "Experimental study of the electro-mechanical switching behavior of a piezoelectric stack actuator," Proceedings of the SPIE, 6929:692907, 2008.

[94] Q. Zhang, W. Pan, A. Bhalla and L.E. Cross, "Electrostrictive and dielectric response in lead magnesium niobate-lead titanate (0.9PMN-0.1PT) and lead lanthanum zirconate titanate (PLZT 9.5/65/35) under variation of temperature and electric field," *Journal of the American Ceramic Society*, 72(4), pp. 599–604, 1989.

[95] W. Zhang and K. Bhattacharya, "A computational model of ferroelectric domains. Part I: model formulation and domain switching," *Acta Materialia*, 53, pp. 185–198, 2005.

[96] D. Zhou, M. Kamlah and D. Munz, "Rate dependence of soft PZT ceramics under electric field loading," Proceedings of the SPIE, 4333, pp. 64–70, 2001.